An improved TROPOMI tropospheric HCHO retrieval over China

Wenjing Su[1*], Cheng Liu[2,3,4,5,6,*], Ka Lok Chan[7], Qihou Hu[2], Haoran Liu[4], Xiangguang Ji[2,8], Yizhi Zhu[2], Ting Liu[1], Chengxin Zhang[1], Yujia Chen[2], Jianguo Liu[2]

[1]School of Earth and Space Sciences, University of Science and Technology of China, Hefei 230026, China

[2]Key Lab of Environmental Optics and Technology, Anhui Institute of Optics and Fine Mechanics, Hefei Institutes of Physical Science, Chinese Academy of Sciences, Hefei 230031, China

[3]Center for Excellence in Regional Atmospheric Environment, Institute of Urban Environment, Chinese Academy of Sciences, Xiamen 361021, China

[4]Department of Precision Machinery and Precision Instrumentation, University of Science and Technology of China, Hefei 230027, China

[5]Key Laboratory of Precision Scientific Instrumentation of Anhui Higher Education Institutes, University of Science and Technology of China, Hefei 230027, China

[6]Anhui Province Key Laboratory of Polar Environment and Global Change, USTC, Hefei 230026, China

[7]Remote Sensing Technology Institute (IMF), German Aerospace Center (DLR), Oberpfaffenhofen, Germany

[8]School of Environmental Science and Optoelectronic Technology, University of Science and Technology of China, Hefei 230026, China

Corresponding author: Cheng Liu (chliu81@ustc.edu.cn) and Ka Lok Chan (ka.chan@dlr.de)

Abstract. We present an improved TROPOspheric Monitoring Instrument (TROPOMI) retrieval of formaldehyde (HCHO) over China. The new retrieval optimizes the slant column density (SCD) retrieval and air mass factor (AMF) calculation for TROPOMI observations of HCHO over China. Retrieval of HCHO differential SCDs (DSCDs) is improved using the basic optical differential spectroscopy (BOAS) technique resulting in lower noise and smaller random error, while AMFs are improved with a priori HCHO profiles from a higher resolution regional chemistry transport model. Compared to the operational product, the new TROPOMI HCHO retrieval shows better agreement with ground based Multi-AXis Differential Optical Absorption Spectroscopy (MAX-DOAS) measurements in Beijing. The improvements are mainly related to the AMF calculation with more precise a priori profiles in winter. Using more precise a priori profiles in general reduces HCHO VCDs by 52.37 % ($\pm$ 27.09 %) in winter. Considering aerosol effect in AMF calculation reduces operational product by 11.46 %

(± 1.48 %) and our retrieval by 17.61 % (± 1.92 %) in winter. The improved and operational HCHO are also used to investigate the spatial-temporal characteristic of HCHO over China. The result shows that both improved and operational HCHO VCDs reach maximum in summer and minimum in winter. High HCHO VCDs mainly located over populated areas, i.e., Sichuan Basin, Central and Eastern China, indicating a significant contribution of anthropogenic emissions. The hotspots are more obvious in the map of the improved HCHO than operational product. The result indicates the improved TROPOMI HCHO is more suitable for the analysis of regional and city scale pollution in China.

1 Introduction

Formaldehyde (HCHO) is an important trace gas playing a crucial role in atmospheric chemistry process. Hydroxyl radicals ($HO_x = OH+HO_2$) produced from HCHO photolysis show a strong influence on the oxidative capacity of the atmosphere (Li et al., 2011; Xue et al., 2016), and contribute to the formation of secondary organic aerosol (SOA) (Jang and Kamens, 2001). Atmospheric HCHO can be emitted from both primary and secondary sources. Primary emissions include industrial sources, vehicle emissions (Wei et al., 2008), biogenic emissions from vegetation and biomass burning (Bauwens et al., 2016). The contribution of secondary sources to ambient HCHO sources is in general much higher than the primary emissions, especially in summer (Su et al., 2019). Secondary HCHO is formed through the oxidation of almost all volatile organic compounds (VOCs). Therefore, it is usually regarded as an indicator of VOCs and being used to analyze sensitivity regimes of ozone (O_3) formation (Martin et al., 2004; Choi et al., 2012; Jin and Holloway, 2015; Liu et al., 2016). Accurate HCHO measurement is important for the investigation of HCHO and O_3 interactions and for the understanding of atmospheric chemistry process. Satellite observations provide indispensable information on HCHO spatial distribution. Satellite observations of HCHO have been conducted since 1996 with a series of satellite borne instruments (Bovensmann et al., 1999; Martin et al., 2004; De Smedt et al., 2012; Barkley et al., 2013; González Abad et al., 2015; González Abad et al., 2016). TROPOspheric Monitoring Instrument (TROPOMI) was launched on 13 October 2017. Compared to its predecessor satellite instruments, TROPOMI provides HCHO observations with a much higher spatial resolution with daily global coverage. The high resolution satellite measurement enables us to analyze the finer scale spatio-temporal characteristic of HCHO.

In this study, we have improved the TROPOMI HCHO over China by optimizing the slant column density (SCD) retrieval and

the air mass factor (AMF) calculation. Different from the operational product (De Smedt et al. 2018), our retrieval uses the basic optical differential spectroscopy (BOAS) technique for the differential SCD (DSCD) retrieval. In addition, the AMF calculation is improved by using higher resolution a priori profiles from the regional Weather Research and Forecasting model (WRF-Chem). It takes the fine scale pollution into account and the result is expected to be more realistic for the investigation of spatio-temporal variation of HCHO over China. Vigouroux et al. (2020) has validated the operational TROPOMI HCHO product using ground-based solar-absorption Fourier Transform Infrared (FTIR) HCHO measurements. However, validating and improvement of TROPOMI HCHO observations over China are still necessary. Therefore, we have analyzed the quality of the operational HCHO product in details and further improved TROPOMI HCHO observations over China.

The paper is organized as follows. Section 2 describes all data sets used in this study. Section 3 presents the improved TROPOMI HCHO retrieval algorithm over China. Uncertainties analysis in HCHO VCD retrieval is discussed in Section 4. The comparisons to TROPOMI HCHO VCDs and ground based Multi-AXis Differential Optical Absorption Spectroscopy (MAX-DOAS) are shown in Section 5. Finally, the summary and conclusion are drawn in Section 6.

2 Data Sets

2.1 The TROPOMI instrument

TROPOMI is onboard the Sentinel-5 Precursor (S5P) satellite. The S5P satellite orbits on the near-polar sun-synchronous orbit at an attitude of 824 km with a 17 days repeat cycle and equator-crossing time of 13:30 h local solar time (LST) on the ascending node. A scanning swath of TROPOMI covers a width of 2600 km providing daily global coverage. TROPOMI has four spectrometers for medium wave ultraviolet (UV), long wave ultraviolet combined with visual (UVIS), near infrared (NIR), and short wave infrared (SWIR), covering non-overlapping and non-contiguous wavelengths from 270 to 2385 nm which are divided into eight spectral bands. The Band 3 with wavelength from 320 to 405 nm is used for HCHO retrieval. Radiance in Band 3 is measured by UVIS spectrometer. The detector for UVIS spectrometer is a two-dimensional charge-coupled device (CCDs) with one dimension for wavelengths and the other dimension for across track spatial coverage (450 rows). Earth radiance is collected along the dayside of the earth, while solar irradiance measurements are performed near the North Pole

every 15 orbits, approximately once a day. In the UVIS channel, the spectral resolution and spectral sampling is about 0.5 nm

75   and 0.2 nm, respectively. Individual ground pixels size of radiance measurement is approximately 3.5 km in the across-track

and 7 km (5.5 km since August 2019), with integration time of 1.08 s (0.84 s since August 2019). The Level 1B radiance and

solar irradiance are available at the Copernicus Open Access Hub (https://scihub.copernicus.eu/, last access: 22 May 2019).

2.2 Operational TROPOMI HCHO product

The operational TROPOMI HCHO product is jointly developed at the German Aerospace Center (DLR) and Royal Belgian

80   Institute for Space Aeronomy (BIRA) (available at https://scihub.copernicus.eu/, last access: 22 May 2019). The operational

product is used to compare to the improved TROPOMI HCHO data set over China. The operational product retrieves HCHO

DSCDs using the DOAS spectral fitting technique in the wavelength range of 328.5-359 nm. The DSCD retrieval settings of

the operational product are listed in Table 1. Using earthshine radiance over remote Pacific Ocean as reference significantly

reduces the influence from unresolved spectral structures which could significantly improve the spectral retrieval of weak

85   absorber, i.e., HCHO. Using radiance as reference reduces the fit residual as it already account for the O_3 absorption and Ring

effect. Daily detector row averaged radiance over the equatorial Pacific (latitude from 5°S to 5°N and longitude from 180°W

to 140°W) is used as reference spectra. Due to residual HCHO signals in reference, the differential SCD (DSCD) is retrieved

in spectra fitting. The conversion of DSCD to VCD uses the AMF approach. A priori HCHO profiles are taken from the global

chemistry transport model Tracer Model 5 (TM5-MP) with a spatial resolution of 1° × 1° with 34 vertical layers up to 0.1hpa

90   and spatio-temporally interpolated to the measurement time and location. Information about data sets used in AMF calculation

is also listed in Table 1. In order to remove the residual HCHO signal in the reference spectra, zonal reference sector correction

is applied following the equation:

$$N_v = (N_s + N_{v,0,CTM} \times M_0 - N_{s,0})/M \qquad (1)$$

Where N_v is the vertical column. N_s is the uncorrected DSCDs. $N_{s,0}$ and M_0 is DSCD and AMF of retrieved over the

95   reference sector ([90°S, 90°N], [180°W to 120°W]). $N_{v,0,CTM}$ is the simulated HCHO vertical column of the reference sector.

The operational algorithm assumes M_0 equals to M and the equation (1) can be expressed as:

$$N_v = (N_s - N_{s,0})/M + N_{v,0,CTM} \qquad (2)$$

The latitude dependency is approximated by a polynomial. DSCDs are averaged into a 5° latitude bin and subsequently used to approximate the coefficient of the polynomial. Detail of S5P operational HCHO algorithm can be found in De Smedt et al. (2018).

2.3 Operational TROPOMI cloud product

Cloud parameters used in AMF calculation in our retrieval are from the operational TROPOMI cloud product. Cloud fraction is retrieved using the Optical Cloud Recognition Algorithm (OCRA) and cloud top height (pressure) and optical thickness (albedo) are retrieved using Neural Networks (ROCINN) algorithm using the "Clouds-as-Reflecting-Boundaries" (CRB) model, treating clouds as simple Lambertian surfaces (Loyola et al., 2018). The operational TROPOMI cloud product is also available at the Copernicus Open Access Hub (https://scihub.copernicus.eu/, last access: 22 May 2019).

2.4 WRF-Chem model

In our retrieval, the chemistry transport model WRF-Chem is used to simulate a priori HCHO profile over China (Su et al., 2017; Zhang et al., 2019; Zhang et al., 2020). Compared to TM5-MP, the regional WRF-Chem simulation has higher spatial resolution of 20×20 km^2. WRF-Chem simulates air pollutions at 44 vertical layers extending from the ground up to 50 hPa. The initial and boundary conditions of the meteorological field for simulation are taken from the National Centers for Environmental Prediction (NCEP) 6-hour Final Operational Global (FNL) reanalysis data with spatial and temporal resolutions of $1° \times 1°$ and 6-hour. The CBMZ (Carbon-Bond Mechanism version Z) photochemical mechanism combined with the MOSAIC (Model for Simulating Aerosol Interactions and Chemistry) aerosol model was used to simulate the chemical process in the atmosphere. WRF-Chem simulations also has more up to date emission inventory over China. The anthropogenic and biogenic emissions are obtained from The Multi-resolution Emission Inventory for China (MEIC) and the Model of Emissions of Gases and Aerosols from Nature (MEGAN) (Guenther et al., 2006; Li et al., 2017), respectively. The MEIC emission inventory has improved the emissions estimation from power plants (Liu et al., 2015), vehicles (Zheng et al., 2014), and residential combustions of non-methane volatile organic compounds (NMVOCs) (Li et al., 2013; Peng et al., 2019). The open burning emission is obtained from the Fire INventory from NCAR (FINN) model (Wiedinmyer et al., 2010). WRF-Chem

simulation is carried out from July 2019 to July 2019 with five days spun up prior to the simulation.

2.5 MAX-DOAS HCHO measurements

MAX-DOAS HCHO measurements are used to validate TROPOMI HCHO observations in this study. The MAX-DOAS measurements are performed at three sites in Beijing (Fig. 1), including one urban and two suburban sites. One suburban site is located in Nancheng (NC) in the southern side of Beijing, while another suburban site is located at the University of Chinese Academy of Sciences (UCAS) in the northeastern side of Beijing. The urban site is located in the Chinese academy of meteorological sciences (CAMS). The locations of three MAX-DOAS sites are indicated in Fig. S1. The distances of three MAX-DOAS sites from city center of Beijing are 8, 27 and 61 km of CAMS, NC, and UCAS sites. The three MAX-DOAS sites are representative of urban and suburban regions of Beijing. The MAX-DOAS instrument consists of a scanning telescope, a stepping motor controlling the viewing direction of the telescope and a spectrometer with Hamamatsu backthinned charge-coupled device (CCD) detector. The spectrometer measures scattered sunlight in the spectral range of 300 - 505 nm. Details of the MAX-DOAS measurement setup are shown in Table 2. Scattered sunlight spectra measured by MAX-DOAS are recoded and analyzed using DOAS Intelligent System (DOASIS) spectral fitting software (Kraus, 2006). Details of the MAX-DOAS HCHO DCSD retrieval settings are listed in Table S1. HCHO vertical profiles are retrieved using Munich Multiple wavelength MAX-DOAS retrieval algorithm (M^3) (Chan et al., 2018). The algorithm is developed based on the optimal estimation method (Rodgers, 2000) and utilizes the radiative transfer model LibRadTran (Emde et al., 2016) as the forward model. In the MAX-DOAS profile retrieval, the lowest 1 km is divided into 10 layers with the thickness of each layer of 100 m, while the thickness of the layers between 1 km and 3 km is set to 200 m. Details of MAX-DOAS HCHO profile retrieval can be found in (Chan et al., 2018; Chan et al., 2019).

3 Improved HCHO retrieval algorithm

The retrieval of HCHO vertical column densities (VCDs) from TROPOMI observations can be separated into three major steps. The first step is the retrieval of HCHO DSCDs. The second step is the reference sector correction, converting DSCDs into SCDs. The final step is the conversion of SCD to VCD using AMF. Details of the improved HCHO retrieval algorithm

are presented in the following.

3.1 HCHO DSCD retrieval

3.1.1 Wavelength calibration

Measured solar irradiances and earthshine radiances are often slightly misaligned with the on ground calibration due to temperature variation of the spectrograph, Doppler shift, non-uniform slit illumination due to presence of clouds or other high reflectance surface. To achieve accurate radiance fitting, it is necessary to calibrate the wavelength mapping before further processing. Irradiance and radiance wavelength are calibrated using a high resolution solar spectrum with accuracy of 0.001 nm (Chance and Kurucz, 2010). The high resolution solar spectrum is convolved with TROPOMI slit function to calculate the solar spectrum with the instrument resolution. This process can be described by Eq. (3):

$$I_r = I_0^h \otimes S(\lambda + \Delta\lambda) \times P_s^m(\lambda) + P_b^m(\lambda) \qquad (3)$$

where I_r is the calculated solar spectrum with the instrument resolution. I_0^h is the high resolution solar spectrum. Λ represents the wavelength. $\Delta\lambda$ indicates the wavelength shift parameter. S is TROPOMI slit function. $\otimes$ represents convolution procedure. $P_s^m(\lambda)$ and $P_b^m(\lambda)$ are scaling and baseline polynomial, respectively, which account for the low-frequency structures of the measured spectra. The polynomial is calculated as:

$$P^m(\lambda) = \sum_{i=0}^{m} C_i(\lambda - \lambda_{avg})^i \qquad (4)$$

where λ_{avg} is the centerwavelength of the fitting window. C_i is the coefficient of the fitted polynomial and m is the order of polynomial. The Full-Width at Half-Maximum (FWHM) and asymmetric factor of the instrument slit function are obtained by fitting the I_r to the measured irradiance using the Gauss-Newton Nonlinear Least Squares (NLLS) method assuming the asymmetric Gaussian shape of slit function. The time series of the fitted TROPOMI slit function parameter from August 2018 to July 2019 in Fig. S2 shows that the TROPOMI slit function is stable after lunch. Therefore, the preflight TROPOMI slit function is used in wavelength calibration procedure. The preflight slit function is obtained from the TROPOMI Calibration Key Data (CKD) (available at http://www.tropomi.eu/data-products/isrf-dataset, last access: 22 May 2019) which is derived

from TROPOMI calibration measurements performed in March 2015 at CSL in Liege. Comparing the spectral fit residual of using different versions of preflight slit function in the spectral fitting, we found that using version v3.0.0 results in lowest residual (Fig. S3). The preflight instrument slit function version v3.0.0 is used in our retrieval, while the operational product uses version v1.0.0 preflight slit function. In the operational algorithm, polynomials are not considered in Eq. (3). In our retrieval, the third order polynomials are selected through sensitivity analysis (Fig. S3). The result shows that using the third order polynomials contributes to reducing residual in wavelength calibration. In wavelength calibration procedure, wavelength shift and coefficients of the polynomials are obtained.

3.1.2 Radiance fitting

HCHO DCSDs are retrieved using the basic optical differential spectroscopy (BOAS) method (Chance, 1998) which has been applied to OMI and OMPS HCHO retrieval (González Abad et al., 2015; González Abad et al., 2016). The BOAS method is based on the direct radiance fit. HCHO DSCDs are determined by fitting the simulated and measured radiance using the NLLS method. The simulated radiance $I_s(\lambda)$ is calculated following the Eq. (5):

$$I_s(\lambda) = \left[\left(aI_0(\lambda + \Delta\lambda) + \alpha_r X_r(\lambda)\right) \times e^{-\sum_j \alpha_j X_j(\lambda)}\right] \times P_s^m(\lambda) + P_b^m(\lambda) \tag{5}$$

where λ represents the wavelength. a is the scaling factor of I_0. $I_0(\lambda + \Delta\lambda)$ denotes the daily average earthshine radiance over the remote Pacific. Radiances measured 1 day before the processing day over the Pacific with latitudes ranging from 30°S to 30°N and longitude ranging from 180°W to 140°W are averaged and used as reference in the spectral fit. $\Delta\lambda$ indicates the wavelength shift parameter. $X_r(\lambda)$ refers to the Raman spectrum (Chance and Spurr, 1997) and α_r is the fitted coefficient to $X_r(\lambda)$. α_j refers to the cross section of trace gas j. Detail of TROPOMI HCHO DSCD retrieval setting is listed in Table 1. Sensitivity analysis is performed to optimize the absorption cross section used in the spectral fit. The sensitivity analysis results are shown in Fig. S4. As expected, considering all absorption cross sections listed in Table 1 significantly reduces fitting residual. Fig. 2 shows the fitted optical depth and residual for two spectra measured on 6 August 2018 over China (orbit 4211). For the spectrum with higher HCHO DSCD, the HCHO absorption can be clearly distinguished in the fitting (see Fig. 2 (a)). The HCHO absorption structures are less significant in the other spectrum as the HCHO DSCD is reaching the detection limit (see Fig. 2 (b)). The detection limit of HCHO DSCD can be expressed by the ratio of root mean square (RMS) to the peak to

190 peak optical density of HCHO in the fitting window (Schönhardt A, 2008). The RMS of fit residual for TROPOMI observation typically varies from 5×10^{-4} to 1×10^{-3}, corresponding to detection limits of HCHO DSCD from $\sim 7 \times 10^{15}$ to $\sim 1 \times 10^{16}$ molec cm^{-2}.

3.2 AMF calculation

HCHO SCDs represent the integration of HCHO concentration along the light path. Therefore, it is strongly dependent on the
195 viewing and solar geometries, surface albedo, and the state of the atmosphere (presence of clouds, vertical HCHO distribution, pressure, temperature, etc). The AMF approach is used to convert SCD to VCD. For optically thin species, the height dependent sensitivity (box AMF) is insensitive to the vertical profile of the species. Therefore, tropospheric HCHO AMF (M) is calculated following the approach of Palmer et al. (2001), which can be described as:

$$M = \frac{\int_{zs}^{zt} w \times n_a dz}{\int_{zs}^{zt} n_a dz} \tag{6}$$

200 where zs and zt are the altitude of surface and the tropopause, respectively. n_a is the partial column of the corresponding layer of the a priori profile, which the a priori profile is taken from the regional WRF-Chem simulation. A priori HCHO profile for TROPOMI AMF calculations are calculated by interpolating WRF-Chem simulation spatio-temporally to the measurement time and location. Box AMF (w) represents the height dependent sensitivity of the TROPOMI measurement. The box AMF depends on wavelength, solar zenith angle (SZA), viewing zenith angle (VZA), relative azimuth angle (RAA), surface albedo,
205 surface pressure, cloud albedo, cloud fraction and cloud pressure. As the wavelength dependency of box AMF in the HCHO fitting windows rather small (less than 5 % for SZA<70°), the box AMF can be calculated at a representative wavelength of 340nm. In order to improve the computational efficiency, the box AMF are pre-calculated using the radiative transfer model VLIDORT (version 2.6) (Spurr, 2008) with a number of surface albedos, surface pressures, solar and viewing geometries and stored in a look up table (LUT). The grid points of these parameters in creating the LUT are same with De Smedt et al (2018).
210 An aerosol free U.S. standard atmosphere is assumed in the radiative transfer calculation of box AMF. Box AMF within the LUT is interpolated into each particular observation condition. Linear interpolation is performed in solar and viewing geometries and surface albedo dimensions and a nearest neighbor interpolation is performed in surface pressure dimension.

Box AMF at each particular observation condition is then linearly interpolated to the pressure level of the a priori HCHO profile.

215 For partly cloudy pixels, cloud correction is applied using the independent pixel approximation (Martin et al., 2002) in which scattering weights of inhomogeneous scenes are considered as a linear combination of box AMF for cloud-free scenes (w_{clear}) and cloudy scene (w_{cloud}) following Eq. (7):

$$w(z) = (1 - CF_{iw}) \times w_{clear} + CF_{iw} \times w_{cloud} \tag{7}$$

where CF_{iw} is the intensity-weighted cloud fraction, defined as:

220
$$CF_{iw} = \frac{C_f \times I_{cloud}}{(1 - C_f) \times I_{clear} + C_f \times I_{cloud}} \tag{8}$$

where C_f is cloud fraction. I_{cloud} and I_{clear} are the radiance intensities for cloudy scene and cloud-free scene, respectively. Radiance intensities are pre-calculated using VLIDORT and saved in the LUT with the same setting as box AMF LUT. Detail information about data sets in AMF calculation is listed in Table 1.

3.3 Reference sector correction

225 Since there are residual HCHO signals in the earthshine reference spectra, therefore, an offset correction has to be applied to the retrieved DSCDs. The first step of reference sector correction is retrieving the DSCDs using average earthshine radiance reference, calculating the corresponding AMFs and storing them as a separate database. The HCHO VCD over remote Pacific Ocean is simulated by GEOS-Chem assuming HCHO over this region is mainly from the oxidation of CH$_4$. The simulated HCHO SCD is calculated by multiplying the VCD (VCD_G) taken from GEOS-Chem with the corresponding AMF (M_0).

230 Assuming HCHO in the reference sector correction is well simulated by GEOS-Chem, the difference between the simulated and retrieved DSCD ($DSCD_0$) is recognized as the DSCD bias caused by residual HCHO signal in reference spectrum. TROPOMI measurements over the Pacific (latitude from 90°S to 90°N and longitude from 160°W to 140°W) are first binned according to their latitude to 500 bins with a resolution of 0.36°. The median value of each bin is then used for the calculation of the DSCD correction (González Abad et al., 2015; González Abad et al., 2016). The DSCD correction (Corr(lat)) can be

235 expressed as the following:

$$Corr(lat) = Median(VCD_G(lat) \times M_0 - DSCD_0) \tag{9}$$

Assuming the DSCD correction is constant in the longitude direction, the DSCD correction at 500 gridded latitude points are linearly interpolated to the latitude of each pixel over China. The interpolated DSCD correction is then applied on the retrieved DSCDs to calculate SCDs. Finally, the HCHO VCDs are calculated as follows:

240

$$VCD = \frac{DSCD + Corr(lat)}{M} = \frac{SCD}{M} \tag{10}$$

We improved the reference sector correction by considering the variability of M_0/M ratio.

4 Uncertainty analysis

Based on equation 10, the uncertainty of VCD can be derived analytically by uncertainty propagation. As VCD retrieval steps in Section 3 are performed independently, their uncertainties are assumed to be uncorrelated. The total uncertainty in HCHO

245 VCD can be expressed following (Boersma et al., 2004; De Smedt et al., 2008):

$$\sigma_{N_V}^2 = (\frac{\partial N_V}{\partial N_S})^2 \sigma_{N_S}{}^2 + (\frac{\partial N_V}{\partial M})^2 \sigma_M{}^2 + (\frac{\partial N_V}{\partial N_{S,0}})^2 \sigma_{N_{S,0}}{}^2 + (\frac{\partial N_V}{\partial N_{V,0,G}})^2 \sigma_{N_{V,0,G}}{}^2 + (\frac{\partial N_V}{\partial M_0})^2 \sigma_{M_0}{}^2 \tag{11}$$

Where N_S is retrieved DSCDs. M and M_0 are both AMFs while M_0 refers to AMF in reference sector. $N_{S,0}$ and $N_{V,0,G}$ are retrieved DSCDs and simulated HCHO VCDs by GEOS in reference sector. σ_{N_S} and σ_M are the uncertainties on DSCD and AMF. $\sigma_{N_{S,0}}$, $\sigma_{N_{V,0,G}}$ and σ_{M_0} are the uncertainties on DSCD, simulated HCHO VCDs and AMF in the reference sector.

250 The Eq. (11) can be transformed into the following equation:

$$\sigma_{N_V}^2 = \frac{1}{M^2}(\sigma_{N_S}{}^2 + \frac{N_S - N_{S,0} + N_{V,0,G} \times M_0}{M^2} \sigma_M{}^2 + \sigma_{N_{S,0}}{}^2 + M_0^2 \sigma_{N_{V,0,G}}{}^2 + N_{V,0,G}^2 \sigma_{M_0}{}^2) \tag{12}$$

4.1 Uncertainties in DSCDs

Uncertainties of DSCD retrieval can be separated into random and systematic uncertainties, and they can be expressed as the following equation.

255

$$\sigma_{N_S}{}^2 = \sigma_{N_{S,rand}}^2 + \sigma_{N_{S,sys}}^2 \tag{13}$$

Random uncertainties are mainly related to instrument noises. Random uncertainties can be approximated by the root mean square (RMS) of spectral fitting residual, the degrees of freedom, and the diagonal term of the covariance matrix for HCHO ($C_{j,j}$):

$$\sigma^2_{N_{S,rand}} = RMS^2 \frac{m}{m-n} C_{j,j}{}^2 \tag{14}$$

260 Where m is the number of spectral pixels and n is the number of fitted parameters. j is index of HCHO cross section in fitting parameters. The covariance matrix ($C_{j,j}$) is calculated from the Jacobian of the forward model corresponding to the fitting parameters (Chan Miller et al., 2014). The mean RMS for measurements taken on 06 August 2018 over the region of 73° E - 130° E, 18° N - 54° N and the corresponding random uncertainty are 5.52×10^{-4} and 0.49×10^{16} molec cm^{-2}, respectively. Systematic uncertainties are mainly from absorption cross sections, choice of fitting window, choice of polynomials and

265 TROPOMI slit function used in the spectral fit. Applying reference sector correction helps to reduce systematic uncertainties significantly. Differences in HCHO SCDs are used to estimate systematic uncertainties. We perform sensitivity analysis to evaluate these effects on HCHO DSCD and SCD retrieval (Table 3). Fitting results using five different fitting windows which are used in previous satellite HCHO retrievals (De Smedt et al., 2008; De Smedt et al., 2012; González Abad et al., 2015) are compared to our result. The effect of using Taylor series of O$_3$ cross section in the spectral retrieval (Puķīte et al., 2010) is

270 also evaluated through sensitivity analysis (Table 3). After reference sector correction, systematic differences regarding to spectral fitting window, polynomials, slit function and Taylor series of O$_3$ cross section (Puķīte et al., 2010) are estimated to be 15.11 %, 2.33 %, 2.33 % and 3.49 %, respectively. Put together with the systematic uncertainty (7 %) caused by absorption cross sections used in the spectral fit González Abad et al. (2016), we estimated the total systematic uncertainty is about 17.3 %.

4.2 Uncertainties in AMF calculations

275 According to Eq. (6), the uncertainties of AMF calculations can be approximated by uncertainty propagation following the equation below.

$$\sigma_M{}^2 = (\frac{\partial M}{\partial a_s} \sigma_{a_s})^2 + (\frac{\partial M}{\partial c_f} \sigma_{c_f})^2 + +(\frac{\partial M}{\partial c_p} \sigma_{c_p})^2 + (\frac{\partial M}{\partial p_h} \sigma_{p_h})^2 \tag{15}$$

Where σ_{a_s}, σ_{c_f}, σ_{c_p} and σ_{p_h} represent the uncertainties of surface albedo (a_s), cloud fraction (c_f), cloud pressure (c_p) and a

priori HCHO profile height (p_h), respectively. A priori HCHO profile height is defined as 75% HCHO is located below this altitude (De Smedt et al. 2018). The observation geometries are measured with high accuracy, therefore, their uncertainties toward AMF uncertainties are negligible. We estimated AMF uncertainties related to surface albedo, cloud fraction, cloud pressure and profile height through sensitivity analysis with a fixed set of observation geometry (SZA=30°, VZA=30°, RAA=0°). Through the sensitivity analysis, we estimated the VCD uncertainty caused by surface albedo, cloud top pressure, cloud fraction and profile height are 0-9 %, 3-10 %, 1-15 % and 1-16 % for clean case and 0-10 %, 3-15 %, 1-11 % and 7-31 % for polluted case, respectively. Details of the error analysis are summarized in table 4. The VCD uncertainty from wavelength dependency of AMF, LUT error, cloud correction and no explicit aerosol correction is about 15-35 % (De Smedt et al. 2018). Considering above uncertainties sources, the VCD uncertainties from AMF calculation are about 17-51 % and 15-43% in polluted and clean cases.

4.3 Uncertainties in reference sector correction

Uncertainty in reference sector correction ($\sigma_{N_{V,0}}$) is caused by HCHO VCD simulation, AMF calculation and SCD retrieval in the reference sector. The uncertainty can be expressed as:

$$\sigma_{N_{V,0}}^2 = \frac{1}{M^2}\left(\sigma_{N_{S,0}}{}^2 + M_0^2\sigma_{N_{V,0,G}}{}^2 + N_{V,0,G}^2\sigma_{M_0}{}^2\right) \tag{16}$$

We take into account the mean standard deviation of simulated HCHO VCD in the reference sector to estimate the uncertainty from model simulation. The uncertainty from VCD simulation is 1.43×10^{16} molec cm^{-2}. The uncertainties from SCD retrieval and AMF calculations in reference sector are calculated same as Eq. (13) and Eq. (15).

5 Results and discussions

5.1 Comparison of operational and improved HCHO product

To analyze the improvement of the new TROPOMI HCHO product, we compared the new HCHO data set to the operational product. The contribution of SCD retrieval and AMF calculation are investigated separately. Both the improved and operation data sets are compared to the MAX-DOAS HCHO measurements to quantify the improvements. The normalized mean bias

(NMB) between satellite and MAX-DOAS data is used as benchmark in the comparison. NMBs between two data sets can be calculated following:

$$NMB = \frac{\sum_{i=1}^{i=n}(V_T(i) - V_M(i))}{\sum_{i=1}^{i=n} V_M(i)} \times 100\% \tag{17}$$

Where $V_T(i)$ and $V_M(i)$ is the average tropospheric HCHO VCD measured by TROPOMI and MAX-DOAS on day i, respectively. The standard error (SE) is calculated by dividing the standard deviation (SD) by the square root of the sample size ($SE = SD/\sqrt{n}$). The two times SE (95% confidence interval (Streiner, 1996)) is regarded as the error of the NMBs in this study. The NMBs larger than the error are considered statistically significant. The error of NMB is calculated following:

$$Error_{NMB} = 2 \times SE = 2 \times \sqrt{\frac{1}{n(n-1)} \frac{\sum_{i=1}^{i=n}\left(V_T(i) - V_M(i) - \overline{V_T(i) - V_M(i)}\right)^2}{\left(\sum_{i=1}^{i=n} V_M(i)/n\right)^2}} \times 100\% \tag{18}$$

MAX-DOAS measurements are temporally averaged within ± 1 h around the TROPOMI overpass time, while TROPOMI pixels within 20 km of the MAX-DOAS site are spatially averaged for comparison. TROPOMI pixels in our retrieval and operational product are both filtered for intensity-weighted cloud fraction smaller than 0.3, root mean square of spectral fit residual (RMS) smaller than 10^{-3}, AMF larger than 0.1 and SZA smaller than 70°, quality assurance value (QA value) larger than 0.55 and successful SCD retrieval. The histograms showing the distributions of RMS of spectral fit of the operational product and our retrieval on 06 August 2018 over China are shown in Figure. S5. About 15 % and 17 % of measurements in the operational product and our retrieval show RMS larger than 10^{-3}.

5.1.1 SCD retrieval

In this section, we compare DSCDs and SCDs after applying reference sector correction between operational product and the new retrieval. The improved TROPOMI HCHO is retrieved using the BOAS approach, while the operational product uses the DOAS technique to retrieve the HCHO DSCDs. Both data sets are filtered for RMS smaller than 10^{-3}. Fig. 4 (a) and (c) shows the TROPOMI HCHO DSCDs retrieved by BOAS and DOAS methods. HCHO DSCDs from both data sets show very similar spatial pattern over China with higher values over industrialized region such as, Beijing-Tianjin-Hebei region (BTH), Yangtze River Delta (YRD), Pearl River Delta (PRD) and Sichuan Basin (SCB). However, the DOAS DSCDs show more scattered

outliers while the BOAS data set show a smoother appearance. As the anthropogenic VOC emission in Tibet is small (Wu et al., 2016; Li et al., 2017) and the oxidation of VOCs is a significant source of HCHO, HCHO in this region is expected to have small spatial variation. The averaged HCHO DSCD of the BOAS retrieval is 0.076×10^{16} molec cm^{-2} with a standard deviation (SD) of 0.51×10^{16} molec cm^{-2} over Tibet (area indicated with blue line), while the DOAS dataset shows higher averaged column of 0.34×10^{16} molec cm^{-2} as well as standard deviation of 0.66×10^{16} molec cm^{-2}. The numbers of valid satellite measurements over Tibet for BOAS and DOAS retrieval are 22244 and 21987, respectively. Larger standard deviation implies the data set contains more outliers. The DOAS HCHO DSCDs are rather noisy over Shaanxi province and its surrounding regions, while BOAS DSCDs appear to be much smoother with a significant hotspot over Xi'an (provincial capital of Shaanxi). As the spatial distribution of HCHO is expected to be smooth, less noisy DSCDs indicate that the BOAS technique is less sensitive to measurement noise.

The scatter plot of the BOAS and DOAS retrieval of HCHO DSCDs over China on 06 August 2018 is in Fig. 5 (a). The result shows BOAS and DOAS retrievals agree well with each other with Pearson correlation coefficient (R) of 0.80. The slope and offset of the linear least squares regression line are 0.91 and 0.24×10^{16} molec cm^{-2}, respectively. Averaged DSCDs on 06 August 2018 over China retrieved by DOAS and BOAS algorithms are 0.57 ($\pm$ 0.0020) $\times 10^{16}$ molec cm^{-2} and 0.36 ($\pm$ 0.0018) $\times 10^{16}$ molec cm^{-2}, respectively. Averaged DSCD retrieved by DOAS method is 58.33 % higher ($0.21 \pm 0.0012 \times 10^{16}$ molec cm^{-2}) than the BOAS retrieval. On the other hand, RMS comparisons shown in Fig. 5 (c) indicate that averaged RMS of the DOAS retrieval ($6.1 \pm 0.003 \times 10^{-4}$) is slightly higher than that of BOAS retrieval ($5.95 \pm 0.003 \times 10^{-4}$). The biases between DSCDs and RMS in operational product and our retrieval are mainly related to the difference of retrieval method, retrieval settings and selection of reference.

To investigate the impact of selection of earthshine radiance reference, we retrieved HCHO DSCDs using daily detector row averaged radiance over the equatorial Pacific (latitude from 5°S to 5°N and longitude from 180°W to 120°W) as reference using BOAS method. Comparisons of HCHO DSCDs and HCHO SCDs after applying reference sector correction using different earthshine radiance reference are presented in Figure. S6. The retrieved DSCDs using different earthshine radiance reference correlated well (R=0.99, Slope=0.99) and with a difference of 30 % ($0.11 \pm 0.0002 \times 10^{16}$ molec cm^{-2}). The bias is compensated (1.9 %) by the reference sector correction (Figure. S6 (b)). To investigate the impact from retrieval method,

BOAS HCHO DSCDs using same retrieval settings with operational DSCD retrieval are compared with DOAS HCHO DSCDs (Figure. S7). Using same retrieval settings, difference between DOAS HCHO DSCDs and BOAS HCHO DSCDs (27.33 %) is significantly reduced and the remaining difference is due to retrieval algorithm. Besides, smaller difference (4.41 %) in HCHO SCDs indicates that reference sector correction reduces the effect from retrieval method (Figure. S7 (b)).

HCHO SCDs after applying reference sector correction in operational product and in our retrieval also show good agreement with Pearson correlation coefficient (R) of 0.80 (Fig. 5 (b)). The slope and intercept of the linear least squares regression line are 0.92 and 0.03×10^{16} molec cm^{-2}. BOAS and DOAS HCHO SCDs also show very similar spatial pattern and the biases between BOAS and DOAS HCHO SCDs reduce after background correction (Fig. 4 (b) and (d)). Averaged SCD taken from the operational product on 06 August 2018 over China ($0.85 \pm 0.0020 \times 10^{16}$ molec cm^{-2}) is on average 4.49 % lower than our retrieval ($0.89 \pm 0.0018 \times 10^{16}$ molec cm^{-2}).

To evaluate improvement of SCD retrieval, we updated the operational product by using BOAS HCHO SCDs and keeping the AMF unchanged. The NMB of the updated HCHO VCD and operational HCHO VCD are shown in Table 5. The bias between the two data sets is caused by difference in SCD retrieval. The updated and operational product is also compared to the MAX-DOAS observations. In summer, using different SCD retrieval methods results a difference of 7.00 % ($\pm$ 1.71 %) from the TROPOMI operational HCHO VCD. The result shows that using the BOAS HCHO SCDs reduced the underestimation in summer and overestimation in winter of the operational product (Table 5). Besides, the mean random errors relative to BOAS are about 22 % lower than DOAS at three MAX-DOAS sites. The result indicates the BOAS technique provides a slightly more stable retrieval of HCHO SCDs.

5.1.2 AMF calculation

The improved TROPOMI HCHO over China uses a priori profile information from higher resolution regional WRF-Chem simulation, while the operational product uses a priori profile from the global TM5-MP model with 1° × 1° resolution. In AMF calculations, both WRF-Chem and TM5-MP simulations are interpolated to TROPOMI spatial resolution. Interpolated WRF-Chem and TM5-MP simulations within 20 km of the MAX-DOAS site are spatially averaged to compare with MAX-DOAS profiles. MAX-DOAS profiles are temporally averaged in the period 13:30-14:30 (Local Time) within ±1 h around the

TROPOMI overpass time. Fig. 6 (a) and (c) show daily averaged a priori HCHO profiles from WRF-Chem and TM5-MP simulations and MAX-DOAS measured profiles. Besides higher horizontal resolution, WRF-Chem simulation also has a higher vertical spatial resolution compared to TM5-MP data set. Although the difference in vertical resolution only shows negligible effect on box AMF under clear sky condition (Fig. 6 (b)), lower vertical resolution profiles would cause significant impact for cloudy cases due to the interpolation of coarse grid (Fig. 6 (d)). Fig. 7 and Fig. 8 show comparisons of seasonal averaged a priori HCHO profiles from MAX-DOAS, WRF-Chem and TM5-MP simulations at urban (CAMS) and suburban (UCAS) sites in spring (March, April, May), summer (June, July, August), autumn (September, October, November) and winter (December, January, February). A priori HCHO profiles simulated by WRF-Chem are similar to MAX-DOAS measurements, while TM5-MP a priori profiles show a larger difference from the MAX-DOAS measurements. The improvement of WRF-Chem simulations at urban site is more significant than suburban site, which is mainly related to the finer spatial resolution and more up to date emission inventory over China used in the simulations. The bias between simulated and measured HCHO profiles at urban site is larger than that at suburban site, which is mainly due to smaller spatial gradient over suburban areas. The AMFs calculated with WRF-Chem and TM5-MP HCHO profiles as a priori are shown in Fig. 9. The results show a similar spatial pattern. However, WRF-Chem AMF is mostly higher than the one calculated with TM5-MP HCHO profiles. The big differences of two AMFs are mainly occurred in pixels with large cloud fraction. To evaluate influence of a priori HCHO profile on VCD retrieval, we updated operational product by keeping the SCDs unchanged and use a priori profile from WRF-Chem for the AMF calculation. The AMF is calculated following Sect 3.2 and using same parameters with operational algorithm except for a priori HCHO profile. The NMBs between the updated and operational HCHO and MAX-DOAS HCHO are shown in Table 5. The effect of a priori HCHO profile is much larger than that from SCD retrieval in winter. Using a priori HCHO profile from WRF-Chem reduces the bias between TROPOMI and MAX-DOAS by 11.48 % ($\pm$ 8.39 %) in summer and 52.37 % ($\pm$ 27.09 %) in winter. The reduction at urban site in winter is larger than suburban site.

5.2 Comparison between HCHO VCDs observed by MAX-DOAS and TROPOMI

To validate TROPOMI tropospheric HCHO VCD, TROPOMI HCHO VCDs are compared to the MAX-DOAS measurements. The left panels in Fig. 10 show the comparison of TROPOMI HCHO VCDs from our retrieval (red lines) and operational

product (green lines) to the MAX-DOAS HCHO VCDs at three MAX-DOAS sites in Beijing. Our retrieval shows better agreement with MAX-DOAS tropospheric HCHO VCD compared to the operational product. The Pearson correlation coefficients (R) of our retrieval are 0.83, 0.84 and 0.83 at CAMS, UCAS and NC sites, respectively. The corresponding R values of operational product are 0.82, 0.80 and 0.82, which are slightly lower than our retrieval. Besides, the slopes of linear least squares regression lines of our retrieval are 0.77, 0.72 and 0.70 at CAMS, UCAS and NC sites. The corresponding values for the operational retrieval are 0.66, 0.67, and 0.62. In addition, the offsets of linear least squares regression lines of our retrieval are 0.37, 0.20 and 0.37$\times 10^{16}$ molec cm^{-2} at three MAX-DOAS sites, with the corresponding values for operational product of 0.41, 0.31 and 0.47$\times 10^{16}$molec cm^{-2}. The agreement between our retrieval and MAX-DOAS observations (higher Pearson correlation coefficient and the regression line is closer to 1:1 reference line) is in general better than the operational product, suggesting that our retrieval is better than the operational product both in urban and suburban in China.

In order to investigate the influence of HCHO a priori profile in the satellite retrieval, we used the MAX-DOAS HCHO profiles as a priori in our TROPOMI AMF calculation following Sect 3.2. The results show an improvement of correlation and absolute agreements. The Pearson correlation coefficient (R) increases by about 0.03. The linear fitting slopes increase by 0.14 and the offsets decrease by 0.09×10^{16} molec cm^{-2}. We have recalculated HCHO VCD for the operational product by using MAX-DOAS HCHO profiles as a priori profiles. The Pearson correlation coefficient (R) between the recalculated operational product and MAX-DOAS HCHO VCD decreases by 0.02 to 0.79. The slope of the regression line increases by 0.19 to 0.84 with offset reduces by 0.24×10^{16} molec cm^{-2} to 0.15×10^{16} molec cm^{-2}. Although the recalculated TROPOMI operational product shows improved correlation with MAX-DOAS observations, our retrieval using MAX-DOAS measurements as a priori profile still shows a better agreement with MAX-DOAS HCHO VCDs. It also indicates that the BOAS spectral retrieval of SCDs agree better to the ground based observations over China.

The right panels of Fig. 10 show the time series of HCHO VCDs from MAX-DOAS, our retrieval and operational product. HCHO VCDs from our retrieval, operational product and MAX-DOAS show a similar temporal variation pattern, reaching maximum value in summer and minimum value in winter. At CAMS site, HCHO VCDs are underestimated by TROPOMI observations and the underestimation of our retrieval (5.78 ± 3.49 %) is slightly smaller (29.77 ± 22.83 %) than that of the operational product (8.23 ± 3.09 %). At UCAS site, both our retrieval and operational product overestimate HCHO VCDs and

the overestimation of our retrieval (5.22 ± 3.49 %) is smaller (51.44 ± 33.70 %) than that of the operational product (10.75 ± 3.09 %). The overestimation of operational product at UCAS site is opposite to previous study that TROPOMI operational product underestimated HCHO VCDs in Xianghe located at ~ 50 km southeast of Beijing compared to FTIR measurements (Vigouroux et al., 2020). In order to investigate the reason of the overestimation, we separated the data by seasons for comparison at three MAX-DOAS sites (Table 5). In summer, high HCHO columns are due to oxidation of VOCs related to enhanced biogenic emissions. Both our retrieval and operational product underestimate HCHO VCD in summer which is consistent with previous studies (Vigouroux et al., 2020; Chan et al., 2020). As shown in Fig. 7 (b) and Fig. 8 (b), WRF-Chem and TM5-MP model both underestimate HCHO concentration in the lower troposphere in summer and result in an overestimation of AMFs. The vertical HCHO profiles simulated by WRF-Chem model are better match with the one measured by MAX-DOAS in summer compared to TM5-MP. Therefore, our retrieval shows slightly better agreement with the ground based measurements (underestimation of 15.81 ± 2.71%) compared to the operational product (underestimation of 18.33 ± 3.10%) during summer. We have also calculated the AMFs using a priori HCHO profile measured by MAX-DOAS for comparison. The underestimation of our retrieval reduces to 1.39 % (± 2.67%) and the underestimation of operational product reduces to 9.74 % (± 2.78%) by using MAX-DOAS profiles for AMF calculations. In wither, lower HCHO columns ($< 1 \times 10^{16}$ molec cm^{-2}) are mainly related to anthropogenic emissions including vehicle exhaust and industrial emissions. The vertical HCHO profiles simulated by WRF-Chem model are similar to the one measured by MAX-DOAS in winter, while the TM5-MP profiles show larger difference to the MAX-DOAS measurements. Both our retrieval and operational product overestimate HCHO VCDs in winter. The overestimation of our retrieval (11.23 ± 4.61 %) is 63.18 % (± 22.63 %) smaller than operational product (29.08 ± 5.59 %) and the overestimation in urban area (QKY) is smaller than that in suburban areas (UCAS and NC sites). The improvements of our retrieval in winter time are more significant and the improvement at urban site is also more significant than suburban sites in winter, which are mainly related to better anthropogenic emission inventory and the finer spatial resolution over China in WRF-Chem simulations. In order to eliminate effect from a priori HCHO profile, a priori HCHO profiles from MAX-DOAS measurements are used for AMF calculations for comparison. The overestimations at CAMS and NC sites become less significant. The overestimation at UCAS site of our retrieval reduces to 3.94 % (± 6.87 %), while the overestimation of operational product reduces to 10.60 % (± 8.71 %). Our result shows an overestimation of

TROPOMI HCHO VCDs during winter at UCAS site. Our result is different from the previous FTIR comparison study (Vigouroux et al., 2020) which shows TROPOMI underestimated HCHO columns in winter. On the one hand, the pollution conditions at three MAX-DOAS sites are different from the FTIR sites used in Vigouroux et al. (2020). On the other hand, HCHO concentrations in the lower troposphere is lower in winter, resulting a relatively larger portion of HCHO above the MAX-DOAS retrieval height of 3km. Therefore, the MAX-DOAS measurements show an underestimation in winter. Our findings are consistence with the previous study that SCIAMACHY HCHO VCDs are in general lower than FTIR measurements while higher than MAX-DOAS observations (Vigouroux et al. 2009). The remaining overestimation is mainly related to a portion of HCHO above 3 km where the MAX-DOAS is not sensitive. In addition, the TROPOMI retrieval assumes aerosol free atmosphere which might also lead to the overestimations.

5.3 Aerosol effect on TROPOMI HCHO retrieval

Aerosol extinction profiles are also retrieved by the MAX-DOAS. Aerosol optical properties, such as single-scattering albedo (SSA) and Ångström exponent obtained from the Aerosol Robotic Network (AERONET) station in Beijing (https://aeronet.gsfc.nasa.gov/, last access: 22 May 2019) are used as input parameters for the MAX-DOAS aerosol profile retrieval. As the aerosol profiles from MAX-DOAS are retrieved at 360nm, we further converted the profile to 340nm using Ångström exponent obtained from the AERONET measurements. To estimate aerosol effect on TROPOMI HCHO retrieval, we calculate the AMFs using MAX-DOAS measured aerosol extinction profiles using VLIDORT (version 2.6) (Spurr, 2008). The AMFs are applied on the operational product and our retrieval. The TROPOMI HCHO VCDs with and without considering aerosols are compared to MAX-DOAS HCHO VCDs. The comparison results are shown in Figure 10. The results show that considering aerosol in the AMF calculations does not improve the agreement with ground based measurements. Considering aerosol effect in TROPOMI retrieval reduces HCHO VCDs by 11.46 % ($\pm$ 1.48 %) for the operational product and 17.61 % ($\pm$ 1.92 %) for our retrieval in winter. The reduction over urban site is more significant than suburban sites, mainly due to higher aerosol load. Operational product using both HCHO and aerosol extinction profiles from MAX-DOAS shows underestimation of 8.36 % ($\pm$ 4.63 %). Our retrieval using MAX-DOAS HCHO and aerosol extinction profiles for AMF calculation underestimates HCHO VCD by 18.53 % ($\pm$ 4.04 %).

5.4 Spatial-temporal characteristic of HCHO over China

Fig. 11 shows the spatial distribution of HCHO VCDs over China in spring, summer, autumn and winter. HCHO VCDs reach highest values in summer and lowest values in winter over China. This is due to higher biogenic emissions (Guenther et al., 1995; Li and Xie, 2014; Jiang et al., 2019) and secondary formation in summer (Wang et al., 2016; Su et al., 2019). The average HCHO VCDs over China in autumn 2018, winter 2018, spring 2019 and summer 2019 are 0.93, 0.91, 0.98 and 1.21×10^{16} molec cm^{-2}, respectively (Table S3). High HCHO VCDs are mainly occurred in central and eastern China and SCB. Lower HCHO values are observed in the western China. Operational product shows similar spatio-temporal distribution with our retrieval over China while the absolute values are (slight) smaller than our retrieval (Figure 12). In summer, hotspots can be observed over BTH, YRD, PRD, Shandong province, Henan province, Wuhan (Hubei's provincial capital), SCB and cities along Fen nutrient-laden valley in Shaanxi and Shanxi provinces in our retrieval. These hotspot patterns are strongly correlated to the population density and industrial emission pattern indicating a significant anthropogenic contribution. These hotspots are less obvious in the operational product in summer. The distribution of high HCHO VCDs observed in our retrieval over the Xinjiang Uygur Autonomous Region is related to the unique topography and industrial areas. The total industrial VOCs emission over the Xinjiang Uygur Autonomous Region is higher than Shanxi province (Zheng et al., 2017).

6 Conclusions

In this paper, we present an improved TROPOMI HCHO retrieval over China. We mainly improve the retrieval in two aspects, SCD and AMF calculations. The improved HCHO uses the BOAS technique for the retrieval of HCHO DSCDs. Compared to the DOAS retrieval technique used in the operational product, results retrieved with the BOAS technique are less noisy while the spatial pattern of HCHO remains similar. DSCDs retrieval with both BOAS and DOAS correlate well with each other with a correlation coefficient of 0.83 and a linear fitting slope of 0.93. The AMF calculations are improved by using HCHO profiles from the regional chemistry transport model WRF-Chem. The WRF-Chem simulation is featured with higher horizontal and vertical resolution. In addition, the emission inventories used in the model are more up to date. A priori HCHO profiles from WRF-Chem in general agree much better with the MAX-DOAS measurements compared to TM5-MP simulation. The

improvement related to the use of finer resolution a priori profile is more significant at urban site, as it better resolved the spatial gradient over these areas.

495 We also compared the improved and operational TROPOMI HCHO VCDs to MAX-DOAS observations at three MAX-DOAS sites in Beijing. The improved HCHO shows better correlation with MAX-DOAS HCHO VCDs compared to the operational product. The improvement of our HCHO retrieval is significant in winter time, mainly related to the use of better a priori profile. Using different spectral retrieval technique for the retrieval of HCHO slant columns only shows a less significant effect in winter. The bias between the improved TROPOMI HCHO VCDs and MAX-DOAS observations is 63.18 % ($\pm$ 22.63 %)

500 smaller than operational product during winter. Moreover, the improvement at urban site in winter is more important than suburban site. These results suggest our retrieval can better capture the fine scale variation of HCHO in both urban and suburban regions. The improved TROPOMI HCHO VCDs and MAX-DOAS show a similar temporal variation pattern with higher values in summer and lower values in winter, while the operational product shows less pronounced seasonal pattern. The improved and operational products both underestimate HCHO VCDs in summer while overestimate HCHO VCDs in

505 winter. Using MAX-DOAS measurements as a priori HCHO profiles in TROPOMI VCD retrieval improves the correlation and reduces the bias between TROPOMI and MAX-DOAS HCHO VCDs. Considering aerosol effect in AMF calculation reduces operational product by 11.46% ($\pm$ 1.48%) and our retrieval by 17.61% ($\pm$ 1.92%) in winter.

The analysis of HCHO spatial distribution shows higher values over SCB, Central and Eastern China and SCB. Lower HCHO VCDs can be observed over western China. In summer, hotspots can be observed over BTH, YRD, PRD, Shandong province,

510 Henan province, Wuhan (Hubei's provincial capital), SCB and cities along Fen nutrient-laden valley in Shaanxi and Shanxi provinces. These spatial patterns indicate significant anthropogenic contributions of atmospheric HCHO. While these hotspots is less obvious indicating that the improved TROPOMI data set provides a better support for the monitoring and controlling the VOCs related pollution.

Data availability. The data used in this paper is available on request from the corresponding author (chliu81@ustc.edu.cn).

515 *Author contributions.* The first two authors contributed equally. CL and KLC designed and supervised the study and CL also help retrieve the satellite data. WS prepared and analyzed satellite data and wrote the manuscript. QH provided useful comments regarding the results. HL and XJ contributed to providing MAX-DOAS HCHO measurements. YZ and TL help ran

the WRF-Chem model. CZ and YC help prepare satellite retrieval. JL supported the project.

Acknowledgments. This work was supported by grants from the National Key Research and Development Program of China (No. 2018YFC0213104, 2017YFC0210002 and 2016YFC0203302), Anhui Science and Technology Major Project (18030801111), National Natural Science Foundation of China (No. 41722501, 51778596 and 41977184), the Strategic Priority Research Program of the Chinese Academy of Sciences (No. XDA23020301), the National Key Project for Causes and Control of Heavy Air Pollution (No. DQGG0102 and DQGG0205), the National High-Resolution Earth Observation Project of China (No. 05-Y20A16-9001-15/17-2), Natural Science Foundation of Guangzhou Province (No.2016A030310115),Civil Aerospace Technology Advance Research Project (No.Y7K00100KJ) and China Postdoctoral Science Foundation (2020TQ0320). The TROPOMI operational Level-1b product and HCHO product are available at https://scihub.copernicus.eu/.

Competing interests. The authors declare that they have no conflict of interest.

References

Barkley, M. P., De Smedt, I., Van Roozendael, M., Kurosu, T. P., Chance, K., Arneth, A., Hagberg, D., Guenther, A., Paulot, F., and Marais, E.: Top‐down isoprene emissions over tropical South America inferred from SCIAMACHY and OMI formaldehyde columns, Journal of Geophysical Research: Atmospheres, 118, 6849-6868, https://doi.org/10.1002/jgrd.50552, 2013.

Bauwens, M., Stavrakou, T., Müller, J.-F., Smedt, I. D., Roozendael, M. V., Werf, G. R., Wiedinmyer, C., Kaiser, J. W., Sindelarova, K., and Guenther, A.: Nine years of global hydrocarbon emissions based on source inversion of OMI formaldehyde observations, Atmos. Chem. Phys., 16, 10133-10158, https://doi.org/10.5194/acp-16-10133-2016, 2016.

Boersma, K. F., Eskes, H., and Brinksma, E. J.: Error analysis for tropospheric NO_2 retrieval from space, Journal of Geophysical Research, 109, https://doi.org/10.1029/2003JD003962, 2004.

Bovensmann, H., Burrows, J., Buchwitz, M., Frerick, J., Noël, S., Rozanov, V., Chance, K., and Goede, A.: SCIAMACHY: Mission objectives and measurement modes, J Atmos Sci, 56, 127-150, https://doi.org/10.1175/1520-0469 (1999)056<0127:SMOAMM>2.0.CO;2, 1999.

Chan Miller, C., Gonzalez Abad, G., Wang, H., Liu, X., Kurosu, T., Jacob, D. J., and Chance, K.: Glyoxal retrieval from the Ozone Monitoring Instrument, Atmos. Meas. Tech., 7, 3891–3907, https://doi.org/10.5194/amt-7-3891-2014, 2014.

Chan, K., Wiegner, M., Wenig, M., and Pöhler, D.: Observations of tropospheric aerosols and NO2 in Hong Kong over 5 years using ground based MAX-DOAS, Science of the total environment, 619, 1545-1556, https://doi.org/10.1016/j.scitotenv.2017.10.153, 2018.

Chan, K. L., Wang, Z., Ding, A., Heue, K.-P., Shen, Y., Wang, J., Zhang, F., Shi, Y., Hao, N., and Wenig, M.: MAX-DOAS measurements of tropospheric NO_2 and HCHO in Nanjing and a comparison to ozone monitoring instrument observations, Atmos. Chem. Phys., 19, 10051-10071, https://doi.org/10.5194/acp-19-10051-2019, 2019.

Chan, K. L., Wiegner, M., van Geffen, J., De Smedt, I., Alberti, C., Cheng, Z., Ye, S., and Wenig, M.: MAX-DOAS measurements of tropospheric NO2 and HCHO in Munich and the comparison to OMI and TROPOMI satellite observations, Atmos. Meas. Tech., 13, 4499–4520, https://doi.org/10.5194/amt-13-4499-2020, 2020.

Chance, K. V., and Spurr, R. J.: Ring effect studies: Rayleigh scattering, including molecular parameters for rotational Raman scattering, and the Fraunhofer spectrum, Appl Optics, 36, 5224-5230, https://doi.org/10.1364/AO.36.005224, 1997.

Chance, K.: Analysis of BrO measurements from the global ozone monitoring experiment, Geophys Res Lett, 25, 3335-3338, https://doi.org/10.1029/98GL52359, 1998.

Chance, K., and Kurucz, R. L.: An improved high-resolution solar reference spectrum for earth's atmosphere measurements in the ultraviolet, visible, and near infrared, Journal of quantitative spectroscopy and radiative transfer, 111, 1289-1295, https://doi.org/10.1016/j.jqsrt.2010.01.036, 2010.

Chance, K., and Orphal, J.: Revised ultraviolet absorption cross sections of H2CO for the HITRAN database, Journal of Quantitative Spectroscopy and Radiative Transfer, 112, 1509-1510, https://doi.org/10.1016/j.jqsrt.2011.02.002, 2011.

Choi, Y., Kim, H., Tong, D., and Lee, P.: Summertime weekly cycles of observed and modeled NOx and O_3 concentrations as a function of satellite-derived ozone production sensitivity and land use types over the Continental United States, Atmos. Chem. Phys., 12, 6291-6307, https://doi.org/10.5194/acp-12-6291-2012, 2012.

De Smedt, I., Muller, J., Stavrakou, T., Eskes, H., and Van Roozendael, M.: Twelve years of global observations of formaldehyde in the troposphere using GOME and SCIAMACHY sensors, Atmos. Chem. Phys., 8, 4947-4963, https://doi.org/10.5194/acp-8-4947-2008, 2008.

De Smedt, I., Van Roozendael, M., Stavrakou, T., Müller, J., Lerot, C., Theys, N., Valks, P., Hao, N., and Van Der A, R.: Improved retrieval of global tropospheric formaldehyde columns from GOME-2/MetOp-A addressing noise reduction and instrumental degradation issues, Atmos. Meas. Tech., 5, 2933-2949, https://doi.org/10.5194/amt-5-2933-2012, 2012.

De Smedt, I., Theys, N., Yu, H., Danckaert, T., Lerot, C., Compernolle, S., Van Roozendael, M., Richter, A., Hilboll, A., and Peters, E.: Algorithm theoretical baseline for formaldehyde retrievals from S5P TROPOMI and from the QA4ECV project, https://doi.org/10.5194/amt-11-2395-2018, 2018.

Fleischmann, O. C., Hartmann, M., Burrows, J. P., and Orphal, J.: New ultraviolet absorption cross-sections of BrO at atmospheric temperatures measured by time-windowing Fourier transform spectroscopy, Journal of Photochemistry and Photobiology A-chemistry, 168, 117-132, https://doi.org/10.1016/j.jphotochem.2004.03.026, 2004.

González Abad, G., Liu, X., Chance, K., Wang, H., Kurosu, T. P., and Suleiman, R.: Updated Smithsonian Astrophysical Observatory Ozone Monitoring Instrument (SAO OMI) formaldehyde retrieval, Atmos. Meas. Tech., 8, 19-32, https://doi.org/10.5194/amt-8-19-2015, 2015.

González Abad, G., Vasilkov, A., Seftor, C., Liu, X., and Chance, K.: Smithsonian Astrophysical Observatory Ozone Mapping and Profiler Suite (SAO OMPS) formaldehyde retrieval, Atmos. Meas. Tech., 9, 2797-2812, https://doi.org/10.5194/amt-9-2797-2016, 2016.

Guenther, A., Hewitt, C. N., Erickson, D., Fall, R., Geron, C., Graedel, T., Harley, P., Klinger, L., Lerdau, M., and McKay, W.: A global model of natural volatile organic compound emissions, Journal of Geophysical Research: Atmospheres, 100, 8873-8892, https://doi.org/10.1029/94JD02950, 1995.

Guenther, A., Karl, T., Harley, P., Wiedinmyer, C., Palmer, P., and Geron, C.: Estimates of global terrestrial isoprene emissions using MEGAN (Model of Emissions of Gases and Aerosols from Nature), Atmos. Chem. Phys., 6, 3181-3210, https://doi.org/10.5194/acp-6-3181-2006, 2006.

Jang, M., and Kamens, R. M.: Characterization of secondary aerosol from the photo oxidation of toluene in the presence of NO x and 1-propene, Environ Sci Technol, 35, 3626-3639, https://doi.org/10.1021/es010676+, 2001.

590 Jiang, Z., Zheng, X., Zhai, H., Wang, Y., Wang, Q., and Yang, Z.: Seasonal and diurnal characteristics of carbonyls in the urban atmosphere of Changsha, a mountainous city in south-central China, Environ Pollut, 253, 259-267, https://doi.org/10.1016/j.envpol.2019.06.127, 2019.

Jin, X., and Holloway, T.: Spatial and temporal variability of ozone sensitivity over China observed from the Ozone Monitoring Instrument, Journal of Geophysical Research: Atmospheres, 120, 7229-7246, https://doi.org/10.1002/2015JD023250, 2015.

595 Kleipool, Q., Dobber, M., De Haan, J. F., and Levelt, P. F.: Earth surface reflectance climatology from 3 years of OMI data, Journal of Geophysical Research, 113, https://doi.org/10.1029/2008JD010290, 2008.

Kraus, S.: DOASIS: A framework design for DOAS, Ph.D. thesis, University of Heidelberg, Germany, 2006.

Li, H., He, Q., Song, Q., Chen, L., Song, Y., Wang, Y., Lin, K., Xu, Z., and Shao, M.: Diagnosing Tibetan pollutant sources via volatile organic compound observations, Atmos Environ, 166, 244-254, https://doi.org/10.1016/j.atmosenv.2017.07.031, 600 2017.

Li, J., Wang, Z., and Xiang, W.: Daytime atmospheric oxidation capacity of urban Beijing under polluted conditions during the 2008 Beijing Olympic Games and the impact of aerosols, Sola, 7, 73-76, https://doi.org/10.2151/sola.2011-019, 2011.

Li, L., and Xie, S.: Historical variations of biogenic volatile organic compound emission inventories in China, 1981–2003, Atmos Environ, 95, 185-196, https://doi.org/10.1016/j.atmosenv.2014.06.033, 2014.

605 Li, M., Zhang, Q., Streets, D. G., He, K. B., Cheng, Y., Emmons, L. K., Huo, H., Kang, S., Lu, Z., and Shao, M.: Mapping Asian anthropogenic emissions of non-methane volatile organic compounds to multiple chemical mechanisms, Atmos. Chem. Phys., 14, 5617-5638, https://doi.org/10.5194/acp-14-5617-2014, 2013.

Li, M., Zhang, Q., Kurokawa, J., Woo, J., He, K., Lu, Z., Ohara, T., Song, Y., Streets, D. G., and Carmichael, G. R.: MIX: a mosaic Asian anthropogenic emission inventory under the international collaboration framework of the MICS-Asia and HTAP, 610 Atmos. Chem. Phys., 17, 935-963, https://doi.org/10.5194/acp-17-935-2017, 2017.

Liu, F., Zhang, Q., Tong, D., Zheng, B., Li, M., Huo, H., and He, K. B.: High-resolution inventory of technologies, activities, and emissions of coal-fired power plants in China from 1990 to 2010, Atmos. Chem. Phys., 15, 13299-13317, https://doi.org/10.5194/acp-15-13299-2015, 2015.

Liu, H., Liu, C., Xie, Z., Li, Y., Huang, X., Wang, S., Xu, J., and Xie, P.: A paradox for air pollution controlling in China revealed by "APEC Blue" and "Parade Blue", Sci Rep, 6, 34408, https://doi.org/10.1038/srep34408, 2016.

Loyola, D. G., Gimeno García, S., Lutz, R., Argyrouli, A., Romahn, F., Spurr, R. J., Pedergnana, M., Doicu, A., Molina García, V., and Schüssler, O.: The operational cloud retrieval algorithms from TROPOMI on board Sentinel-5 Precursor, Atmos. Meas. Tech., 11, https://doi.org/10.5194/amt-11-409-2018, 2018.

Malicet, J., Daumont, D., Charbonnier, J., Parisse, C., Chakir, A., and Brion, J.: Ozone UV spectroscopy. II. Absorption cross-sections and temperature dependence, J Atmos Chem, 21, 263-273, https://doi.org/10.1007/BF00696758, 1995.

Martin, R., Parrish, D., Ryerson, T., Nicks, D., Chance, K., Kurosu, T., Jacob, D. J., Sturges, E., Fried, A., and Wert, B.: Evaluation of GOME satellite measurements of tropospheric NO_2 and HCHO using regional data from aircraft campaigns in the southeastern United States, Journal of Geophysical Research: Atmospheres, 109, https://doi.org/10.1029/2004jd004869, 2004.

Martin, R. V., Chance, K., Jacob, D. J., Kurosu, T. P., Spurr, R. J., Bucsela, E., Gleason, J. F., Palmer, P. I., Bey, I., and Fiore, A. M.: An improved retrieval of tropospheric nitrogen dioxide from GOME, Journal of Geophysical Research: Atmospheres, 107, ACH 9-1-ACH 9-21, https://doi.org/10.1029/2001JD001027, 2002.

Meller, R., and Moortgat, G. K.: Temperature dependence of the absorption cross sections of formaldehyde between 223 and 323 K in the wavelength range 225–375 nm, Journal of Geophysical Research, 105, 7089-7101, https://doi.org/10.1029/1999JD901074, 2000.

Palmer, P. I., Jacob, D. J., Chance, K., Martin, R. V., Spurr, R. J., Kurosu, T. P., Bey, I., Yantosca, R., Fiore, A., and Li, Q.: Air mass factor formulation for spectroscopic measurements from satellites: Application to formaldehyde retrievals from the Global Ozone Monitoring Experiment, Journal of Geophysical Research: Atmospheres, 106, 14539-14550, https://doi.org/10.1029/2000JD900772, 2001.

Rodgers, C. D.: Inverse methods for atmospheric sounding: theory and practice, World scientific, 2000.

Peng, L., Zhang, Q., Yao, Z., Mauzerall, D. L., Kang, S., Du, Z., Zheng, Y., Xue, T., and He, K.: Underreported coal in statistics: A survey-based solid fuel consumption and emission inventory for the rural residential sector in China, Applied Energy, 235, 1169-1182, https://doi.org/10.1016/j.apenergy.2018.11.043, 2019.

Puķīte, J., Kühl, S., Deutschmann, T., Platt, U., and Wagner, T.: Extending differential optical absorption spectroscopy for limb measurements in the UV, Atmos. Meas. Tech., 3, 631–653, https://doi.org/10.5194/amt-3-631-2010, 2010.

Schönhardt A, R. A., Wittrock F: Observations of iodine monoxide columns from satellite, Atmos. Chem. Phys., https://doi.org/10.5194/acp-8-637-2008, 2008.

Serdyuchenko, A., Gorshelev, V., Weber, M., Chehade, W., and Burrows, J. P.: High spectral resolution ozone absorption cross-sections – Part 2: Temperature dependence, Atmos. Meas. Tech., 7, 625-636, https://doi.org/10.5194/amt-7-625-2014, 2014.

Spurr, R.: LIDORT and VLIDORT: Linearized pseudo-spherical scalar and vector discrete ordinate radiative transfer models for use in remote sensing retrieval problems, in: Light Scattering Reviews 3: Light Scattering and Reflection, edited by: Kokhanovsky, A. A., Springer Berlin Heidelberg, Berlin, Heidelberg, 229-275, 2008.

Streiner, D. L.: Maintaining Standards: Differences between the Standard Deviation and Standard Error, and When to Use Each, The Canadian Journal of Psychiatry, 41, 498-502, https://doi.org/10.1177/070674379604100805, 1996.

Su, W., Liu, C., Hu, Q., Fan, G., Xie, Z., Huang, X., Zhang, T., Chen, Z., Dong, Y., Ji, X., Liu, H., Wang, Z., and Liu, J.: Characterization of ozone in the lower troposphere during the 2016 G20 conference in Hangzhou, Sci Rep-Uk, 7, 17368, https://doi.org/10.1038/s41598-017-17646-x, 2017.

Su, W., Liu, C., Hu, Q., Zhao, S., Sun, Y., Wang, W., Zhu, Y., Liu, J., and Kim, J.: Primary and secondary sources of ambient formaldehyde in the Yangtze River Delta based on Ozone Mapping and Profiler Suite (OMPS) observations, Atmos. Chem. Phys., 19, 6717-6736, https://doi.org/10.5194/acp-19-6717-2019, 2019.

Thalman, R., and Volkamer, R.: Temperature dependent absorption cross-sections of O_2–O_2 collision pairs between 340 and 630 nm and at atmospherically relevant pressure, Phys Chem Chem Phys, 15, 15371-15381, https://doi.org/versity o, 2013.

Vandaele, A. C., Hermans, C., Simon, P. C., Carleer, M., Colin, R., Fally, S., Merienne, M.-F., Jenouvrier, A., and Coquart, B.: Measurements of the NO_2 absorption cross-section from 42000 cm^{-1} to 10000 cm^{-1} (238–1000 nm) at 220 K and 294 K,

Journal of Quantitative Spectroscopy and Radiative Transfer, 59, 171-184, https://doi.org/10.1016/S0022-4073(97)00168-4, 1998.

Vigouroux, C., Hendrick, F., Stavrakou, T., Dils, B., Smedt, I. D., Hermans, C., Merlaud, A., Scolas, F., Senten, C., and Vanhaelewyn, G.: Ground-based FTIR and MAX-DOAS observations of formaldehyde at Réunion Island and comparisons with satellite and model data, Atmos. Chem. Phys., 9, 9523-9544, https://doi.org/10.5194/acp-9-9523-2009, 2009.

Vigouroux, C., Langerock, B., Bauer Aquino, C. A., Blumenstock, T., Cheng, Z., De Mazière, M., De Smedt, I., Grutter, M., Hannigan, J. W., Jones, N., Kivi, R., Loyola, D., Lutsch, E., Mahieu, E., Makarova, M., Metzger, J.-M., Morino, I., Murata, I., Nagahama, T., Notholt, J., Ortega, I., Palm, M., Pinardi, G., Röhling, A., Smale, D., Stremme, W., Strong, K., Sussmann, R., Té, Y., van Roozendael, M., Wang, P., and Winkler, H.: TROPOMI–Sentinel-5 Precursor formaldehyde validation using an extensive network of ground-based Fourier-transform infrared stations, Atmos. Meas. Tech., 13, 3751–3767, https://doi.org/10.5194/amt-13-3751-2020, 2020.

Wang, D., Zhou, B., Fu, Q., Zhao, Q., Zhang, Q., Chen, J., Yang, X., Duan, Y., and Li, J.: Intense secondary aerosol formation due to strong atmospheric photochemical reactions in summer: observations at a rural site in eastern Yangtze River Delta of China, Science of the Total Environment, 571, 1454-1466, https://doi.org/10.1016/j.scitotenv.2016.06.212, 2016.

Wei, W., Wang, S., Chatani, S., Klimont, Z., Cofala, J., and Hao, J.: Emission and speciation of non-methane volatile organic compounds from anthropogenic sources in China, Atmos Environ, 42, 4976-4988, https://doi.org/10.1016/j.atmosenv.2008.02.044, 2008.

Wiedinmyer, C., Akagi, S. K., Yokelson, R. J., Emmons, L. K., Alsaadi, J. A., Orlando, J. J., and Soja, A. J.: The Fire INventory from NCAR (FINN): a high resolution global model to estimate the emissions from open burning, Geosci Model Dev, 4, 625-641, https://doi.org/10.5194/gmd-4-625-2011, 2010.

Wilmouth, D. M., Hanisco, T. F., Donahue, N. M., and Anderson, J. G.: Fourier transform ultraviolet spectroscopy of the A 2Π3/2← X 2Π3/2 transition of BrO, The journal of physical chemistry a, 103, 8935-8945, https://doi.org/10.1021/jp991651o, 1999.

Wu, R., Bo, Y., Li, J., Li, L., Li, Y., and Xie, S.: Method to establish the emission inventory of anthropogenic volatile organic compounds in China and its application in the period 2008–2012, Atmos Environ, 127, 244-254, https://doi.org/10.1016/j.atmosenv.2015.12.015, 2016.

Xue, L., Gu, R., Wang, T., Wang, X., Saunders, S., Blake, D., Louie, P. K., Luk, C. W., Simpson, I., and Xu, Z.: Oxidative capacity and radical chemistry in the polluted atmosphere of Hong Kong and Pearl River Delta region: analysis of a severe photochemical smog episode, Atmos. Chem. Phys., https://doi.org/10.5194/acp-16-9891-2016, 2016.

Zhang, C., Liu, C., Hu, Q., Cai, Z., Su, W., Xia, C., Zhu, Y., Wang, S., and Liu, J.: Satellite UV-Vis spectroscopy: implications for air quality trends and their driving forces in China during 2005–2017, Light: Science & Applications, 8, 100, https://doi.org/10.1038/s41377-019-0210-6, 2019.

Zhang, C., Liu, C., Chan, K. L., Hu, Q., Liu, H., Li, B., Xing, C., Tan, W., Zhou, H., Si, F., and Liu, J.: First observation of tropospheric nitrogen dioxide from the Environmental Trace Gases Monitoring Instrument onboard the GaoFen-5 satellite, Light: Science & Applications, 9, 66, https://doi.org/10.1038/s41377-020-0306-z, 2020.

Zheng, B., Huo, H., Zhang, Q., Yao, Z., Wang, X., Yang, X., Liu, H., and He, K. B.: High-resolution mapping of vehicle emissions in China in 2008, Atmos. Chem. Phys., 14, 9787-9805, https://doi.org/10.5194/acp-14-9787-2014, 2014.

Zheng, C., Shen, J., Zhang, Y., Huang, W., Zhu, X., Wu, X., Chen, L., Gao, X., and Cen, K.: Quantitative assessment of industrial VOC emissions in China: Historical trend, spatial distribution, uncertainties, and projection, Atmos Environ, 150, 116-125, https://doi.org/10.1016/j.atmosenv.2016.11.023, 2017.

Zhou, Y., Brunner, D., Boersma, K. F., Dirksen, R., and Wang, P.: An improved tropospheric NO2 retrieval for OMI observations in the vicinity of mountainous terrain, Atmos. Meas. Tech., 2, 401-416, https://doi.org/10.5194/amt-2-401-2009, 2009.
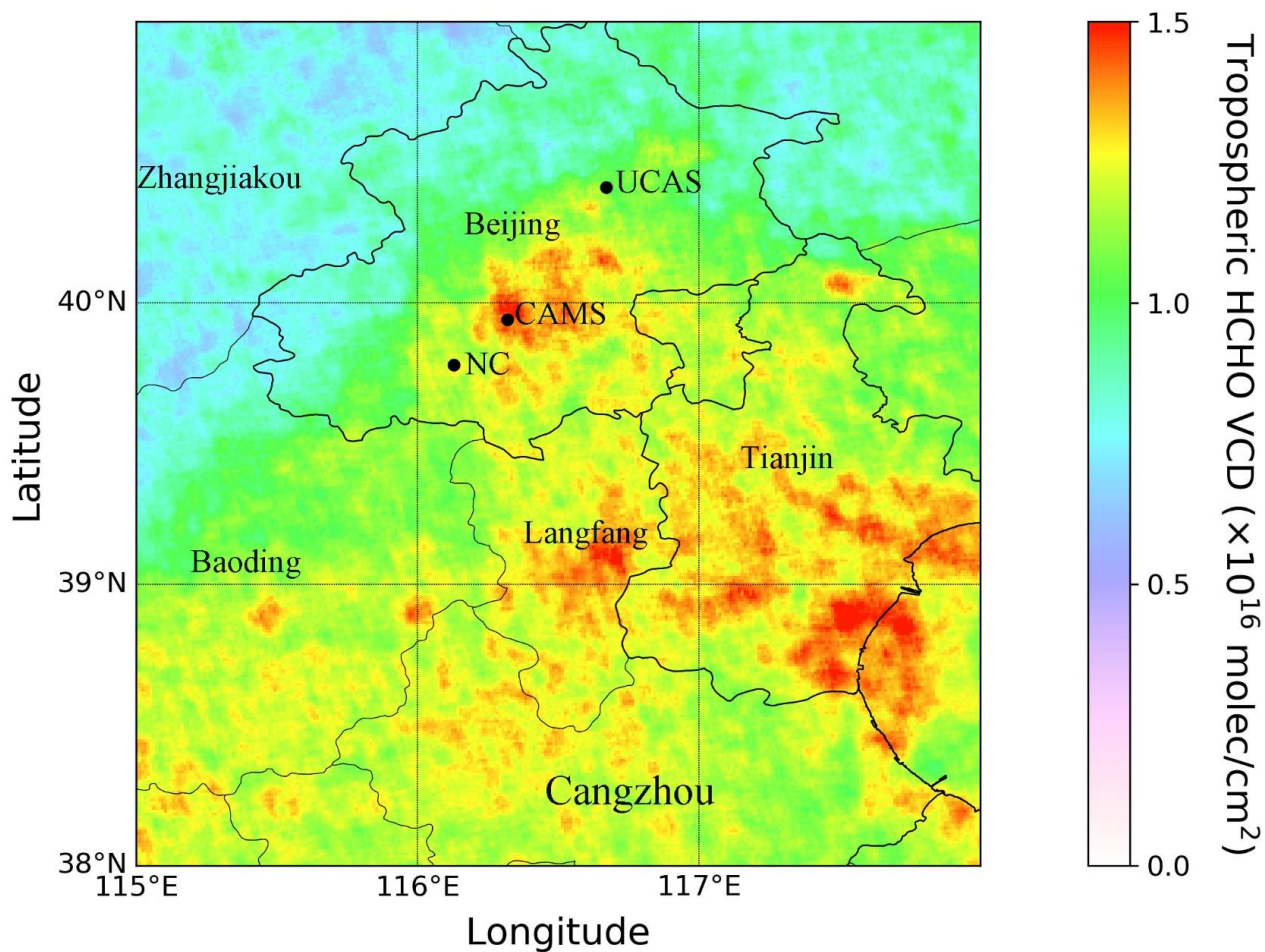
Figure 1. Annual average of the improved TROPOMI tropospheric HCHO VCD from August 2018 to July 2019 in Beijing and its surrounding region on a 0.01°×0.01° grid. The black dots indicate the locations of MAX-DOAS sites.

Table 1. The retrieval settings for TROPOMI HCHO DSCD and information used in AMF calculations in operational product and our retrieval.

	Operational product (De Smedt et al. 2018)	Our retrieval
SCD retrieval		
algorithm	DOAS	BOAS
Fitting window	328.5-359 nm	328.5-359 nm

Radiance reference spectrum	Daily average of radiances of the Pacific orbit between 5°S and 5°N, 180 °W and 120 °W	Daily average of radiances of the Pacific orbit between 30°S and 30°N, 180 °W and 140 °W
Polynomial	5th order	Scaling polynomial: 3rd order Baseline polynomial: 3rd order
Instrument slit function	TROPOMI ISRF Calibration Key Data (CKD) v1.0.0	TROPOMI ISRF Calibration Key Data (CKD) v3.0.0
Solar reference spectrum	(Chance and Kurucz, 2010)	(Chance and Kurucz, 2010)
Ring effect	Ring cross section (Chance and Spurr, 1997)	Raman spectrum (Chance and Spurr, 1997)
HCHO cross sections	(Meller and Moortgat, 2000), 298K	(Chance and Orphal, 2011) , 300K
O_3 cross sections	(Serdyuchenko et al., 2014), 223 and 243K	(Malicet et al., 1995) , 228 and 295K, I_0 corrected
NO_2 cross sections	(Vandaele et al., 1998) , 220K	(Vandaele et al., 1998) , 220K
BrO cross sections	(Fleischmann et al., 2004), 223K	(Wilmouth et al., 1999) , 228K
O_4 cross sections	(Thalman and Volkamer, 2013) , 293K	(Thalman and Volkamer, 2013) , 293K
AMF calculations		
Altitude-dependent AMFs	VLIDORT, 340 nm, 6-D AMF look-up table	VLIDORT, 340 nm, 6-D AMF look-up table
Cloud parameter	S5P operational cloud product(see Sect. 2.2)	Same as left
Treatment of partly cloudy scenes	IPA, no correction for f_{eff}<10%	Same as left
Surface albedo	OMI-based monthly minimum LER at 342 nm (Kleipool et al., 2008)	Same as left
A priori HCHO profile	TM5-MP daily forecast with the spatial resolution of 1°×1° (lat×long)	WRF-Chem daily simulations with the spatial resolution of 20×20 km^2
Aerosols	No explicit correction	Same as left

710

Table 2. Information of the MAX-DOAS measurements. Viewing azimuth angle of the north is taken as zero degree. Relative error is calculated by mean of relative errors of MAX-DOAS measurements within ±1 h around the TROPOMI overpass time.

Site name	Location	Region	Height	viewing azimuth	elevation	Relative	Available

			above sea level (m)	angle (°)	angles(°)	error	days
CAMS	39.94° N, 116.32° E	urban area	100	130 (southeast)	1, 2, 3, 4, 5, 6, 8, 10, 15, 30, 90	14.32%	352
UCAS	40.41° N, 116.67° E	suburb	120	67 (northeast)	1, 2, 3, 4, 5, 6, 8, 10, 15, 30, 90	14.03%	321
NC	39.78° N, 116.13° E	suburb	60	48 (northeast)	1, 2, 3, 4, 5, 6, 8, 10, 15, 30, 90	19.00%	331
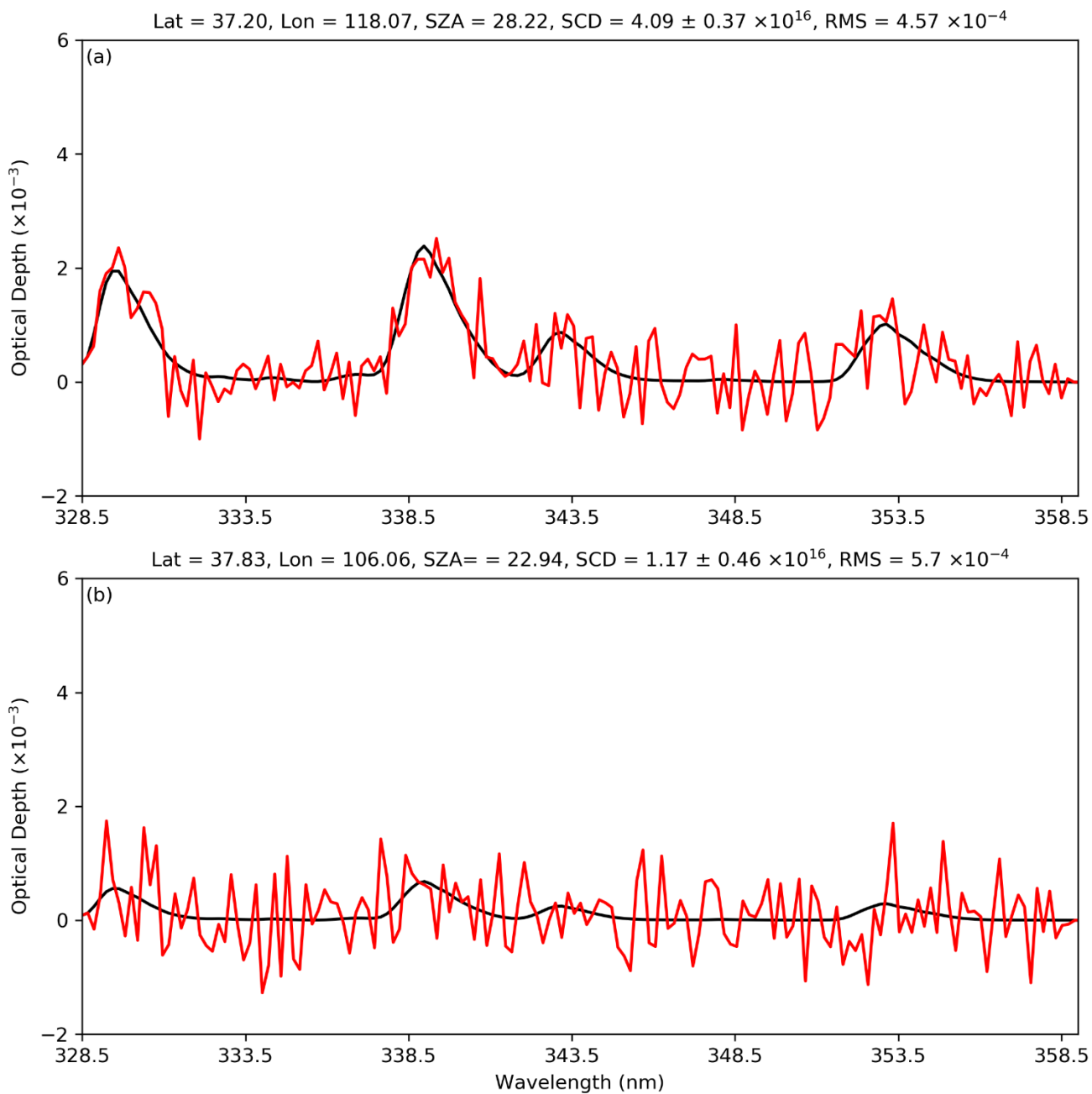
715

Figure 2. An example of the spectral retrieval of HCHO DSCD from two TROPOMI spectra measured on 6 August 2018 over China (orbit 4211), for (a) polluted case and (b) clean case. The black lines represent the simulated HCHO optical depth, and the red lines represent the fitted HCHO optical depth plus fitting residuals.

720 **Table 3. Parameter effects on daily mean HCHO DSCDs and SCDs, ±1 standard deviation of DSCDs ($\pm 1\sigma_D$) and SCDs ($\pm 1\sigma_S$), and mean root mean square (RMS) of spectral fitting residual on 06 August 2018 of the region between 73° E and 130° E, and 18° N and 54° N. Units of DSCDs, SCDs, $\pm 1\sigma_D$ and $\pm 1\sigma_S$ are $\times 10^{16}$ molec cm^{-2}. RMS units are $\times 10^{-4}$. The detailed retrieval settings for reference case are listed in the column with the header of "Our retrieval" in Table 1. The rows below "Reference case" with specific settings are modified with respect to the reference case while all other settings are kept unchanged.**

Retrieval settings	DSCDs	$\pm 1\sigma_D$	RMS	SCDs	$\pm 1\sigma_S$
Reference case	0.34	$\pm$ 0.57	5.84	0.86	$\pm$ 0.58
328.5-346.0 nm	0.46	$\pm$ 0.96	5.83	0.87	$\pm$ 0.96
328.5-356.5 nm	0.38	$\pm$ 0.62	5.88	0.88	$\pm$ 0.63
337.0-353.0 nm	0.49	$\pm$ 1.65	5.69	0.99	$\pm$ 1.65
337.5-359.0 nm	0.40	$\pm$ 0.99	5.84	0.82	$\pm$ 0.99
334.0-348.0 nm	0.28	$\pm$ 2.43	5.60	0.74	$\pm$ 2.43
4th order baseline and scaling polynomials	0.41	$\pm$ 0.65	6.00	0.88	$\pm$ 0.67
TROPOMI ISRF Calibration Key Data (CKD) v1.0.0	0.34	$\pm$ 0.61	6.04	0.88	$\pm$0.61
The first order Taylor series approach for O_3 SCDs (Puķīte et al., 2010)	0.33	$\pm$0.63	6.04	0.83	$\pm$0.65

725
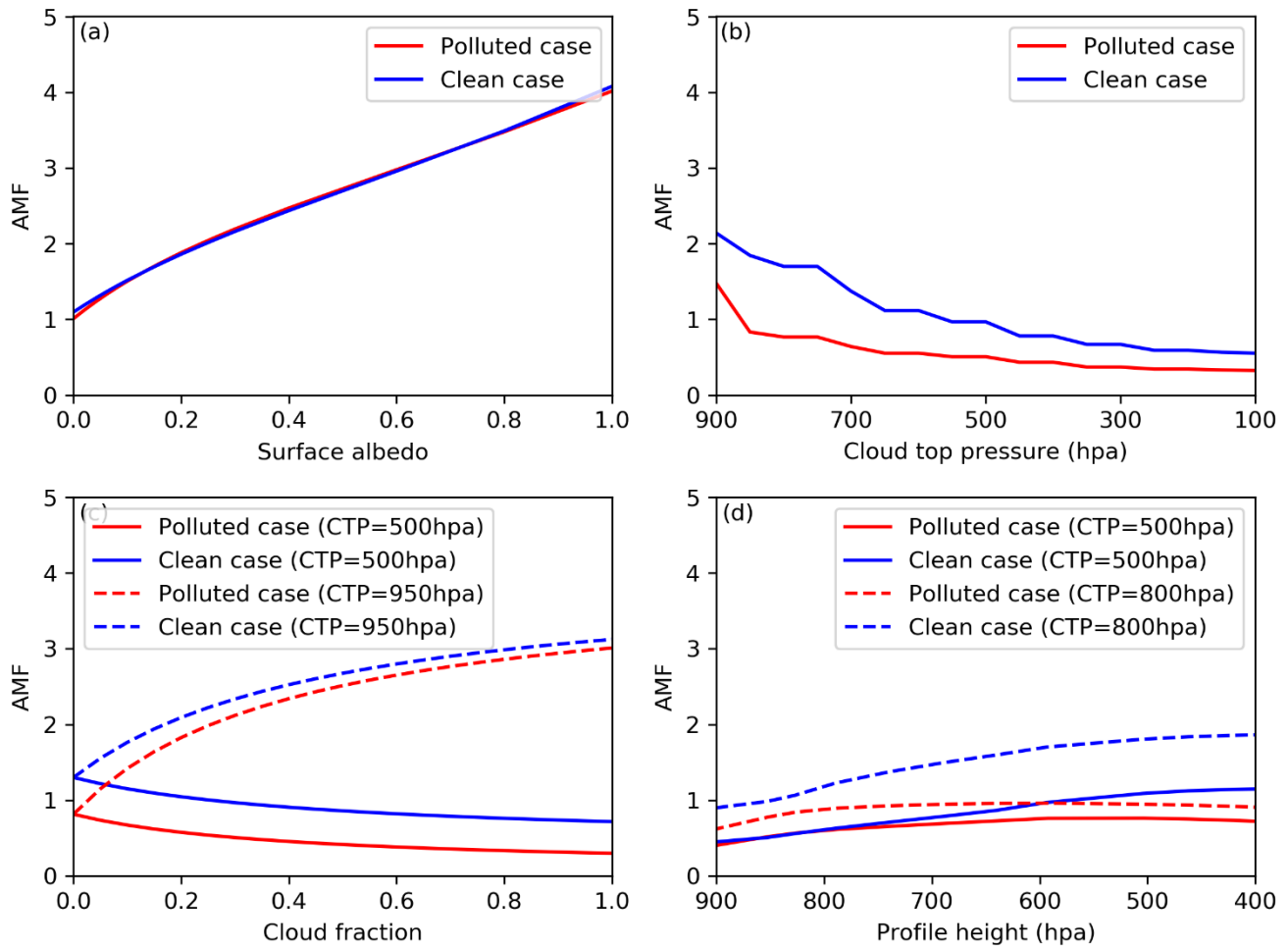
Figure 3. AMF variations with surface albedo (a), cloud top pressure (b), cloud fraction (c) and profile height (d) over clean and polluted cases. In panel (a), cloud fraction is 0. In panel (b) and (d), cloud fractions are 0.3 and surface albedos are 0.05.

730 **Table 4. Uncertainties of TROPOMI HCHO VCD from the parameters used in AMF calculation. Uncertainties are estimated with a fixed set of observation geometry (SZA=30°, VZA=30°, RAA=0°).**

Uncertainty source	Clean area	Polluted area
Surface albedo	0-9%	0-10%
Cloud top pressure	3-10%	3-15%
Cloud fraction	1-15%	1-11%
Profile height	1-16%	7-31%

AMF LUT and no explicit aerosol correction	15-35%(De Smedt et al. 2018)	15-35%(De Smedt et al. 2018)
Total	15-43%	17-51%
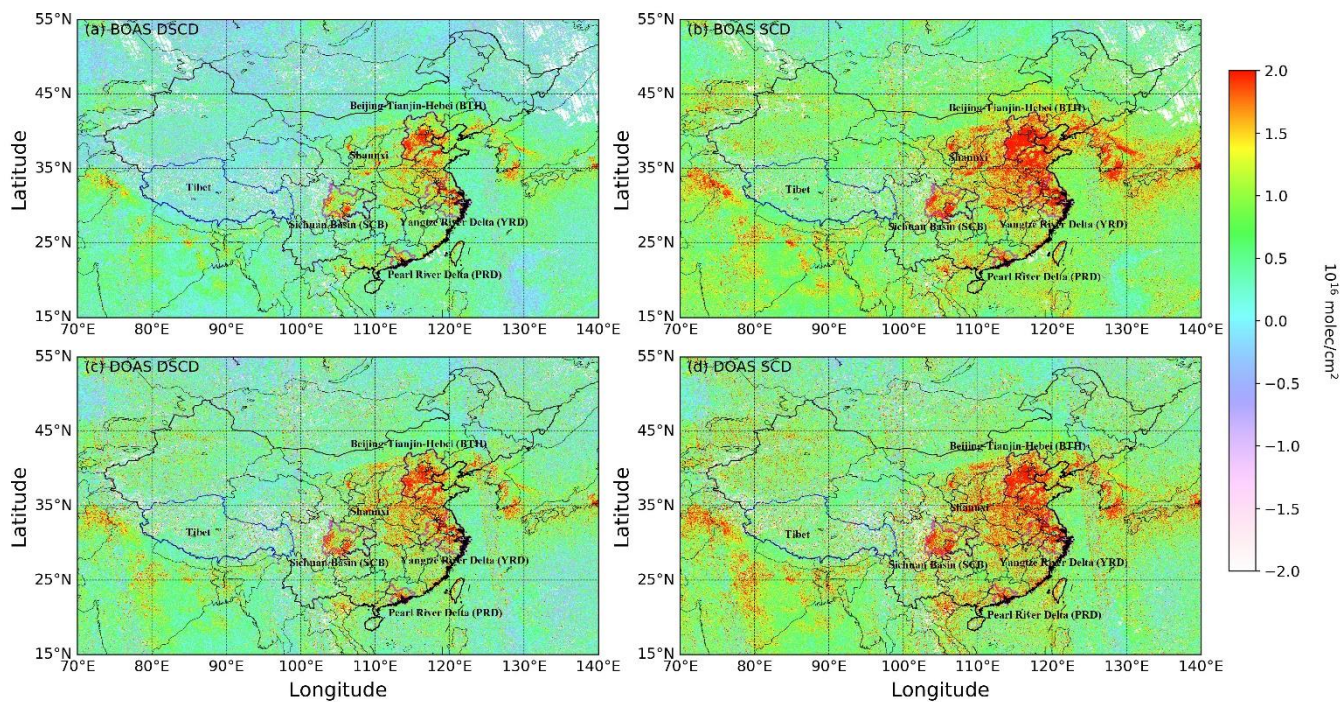
Figure 4. Spatial distributions of BOAS (a) and DOAS (c) HCHO DSCDs and BOAS (b) and DOAS (d) HCHO SCDs on 06 August 2018 over China from orbit 04210 to orbit 04213. The regional boundaries of BTH, YRD, PRD and SCB are delineated by magenta lines.
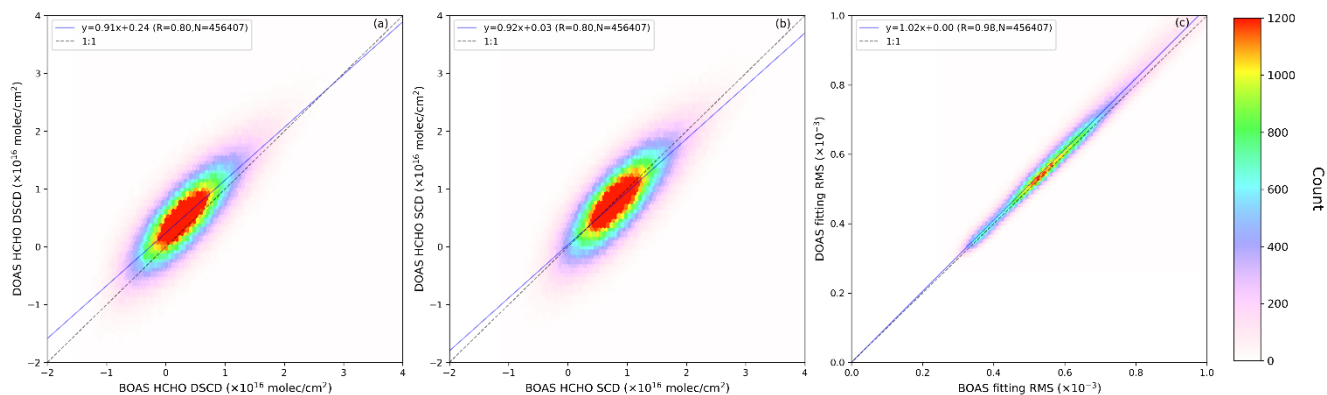
Figure 5. (a) Pixel to pixel comparisons of DOAS and BOAS HCHO DSCDs, (b) DOAS and BOAS HCHO SCDs and (c) DOAS and BOAS fitting RMS on 06 August 2018 in the region between 73° E and 130° E, and 18° N and 54° N.

Table 5. Normalized mean biases (NMBs) between the updated and operational TROPOMI HCHO VCDs (NMB$_{U,O}$) and NMBs between TROPOMI and MAX-DOAS observations (NMB$_{T,M}$). TROPOMI HCHO VCDs are updated with three different settings, (1) replacing DOAS SCDs using BOAS SCDs in the operational product, (2) changing the a priori profiles from TM5-MP to regional WRF-Chem simulations in the operational product and (3) both (1) and (2) changes in the operational product. The error bars ($\pm$ Error$_{NMB}$) are also presented. The NMBs and theirs errors are calculated following Eq. (17) and Eq. (18) respectively. All values are in %.

Settings		CAMS		UCAS		NC	
		NMB$_{U,O}$	NMB$_{T,M}$	NMB$_{U,O}$	NMB$_{T,M}$	NMB$_{U,O}$	NMB$_{T,M}$
Operational product (DOAS & TM5-MP)	Year	-	-8.23±3.09	-	10.75±4.82	-	3.73±3.77
	Summer	-	-14.92±5.03	-	-21.96±5.31	-	-18.12±5.73
	Winter	-	20.28±8.74	-	44.10±11.27	-	22.87±8.82
BOAS & TM5-MP	Year	0.20±3.24	-9.85±4.57	-0.43±2.95	15.33±4.84	-1.50 ± 2.24	2.48±3.59
	Summer	3.91±1.89	-11.69±4.94	10.00±3.90	-14.16±5.01	7.20 ±2.74	-12.23±5.33
	Winter	-2.67±4.31	18.98±10.15	-4.15±11.54	36.19±18.44	-3.75 ± 9.56	18.12±17.44

DOAS & WRF-Chem	Year	7.86±2.84	-7.10±6.58	-9.49±3.25	6.70±3.19	-5.61±2.73	-2.83±3.29
	Summer	1.12±4.47	-13.80±7.76	5.15±4.81	-18.66±4.57	3.13±4.87	-15.96±5.19
	Winter	-17.83±8.00	10.38±9.36	-15.19±8.66	20.44±11.95	-14.26±2.70	10.37±9.01
BOAS & WRF-Chem	Year	2.61±1.87	-5.78±3.49	-10.77± 2.11	5.22±4.10	-6.42±1.75	-3.30±3.29
	Summer	3.18±3.41	-12.21±4.81	3.65 ± 5.53	-17.87±4.43	0.27±3.60	-17.34±4.82
	Winter	-13.87±2.93	6.38±6.35	-11.89 ± 3.22	19.38±11.44	-12.56±3.46	7.94±4.45
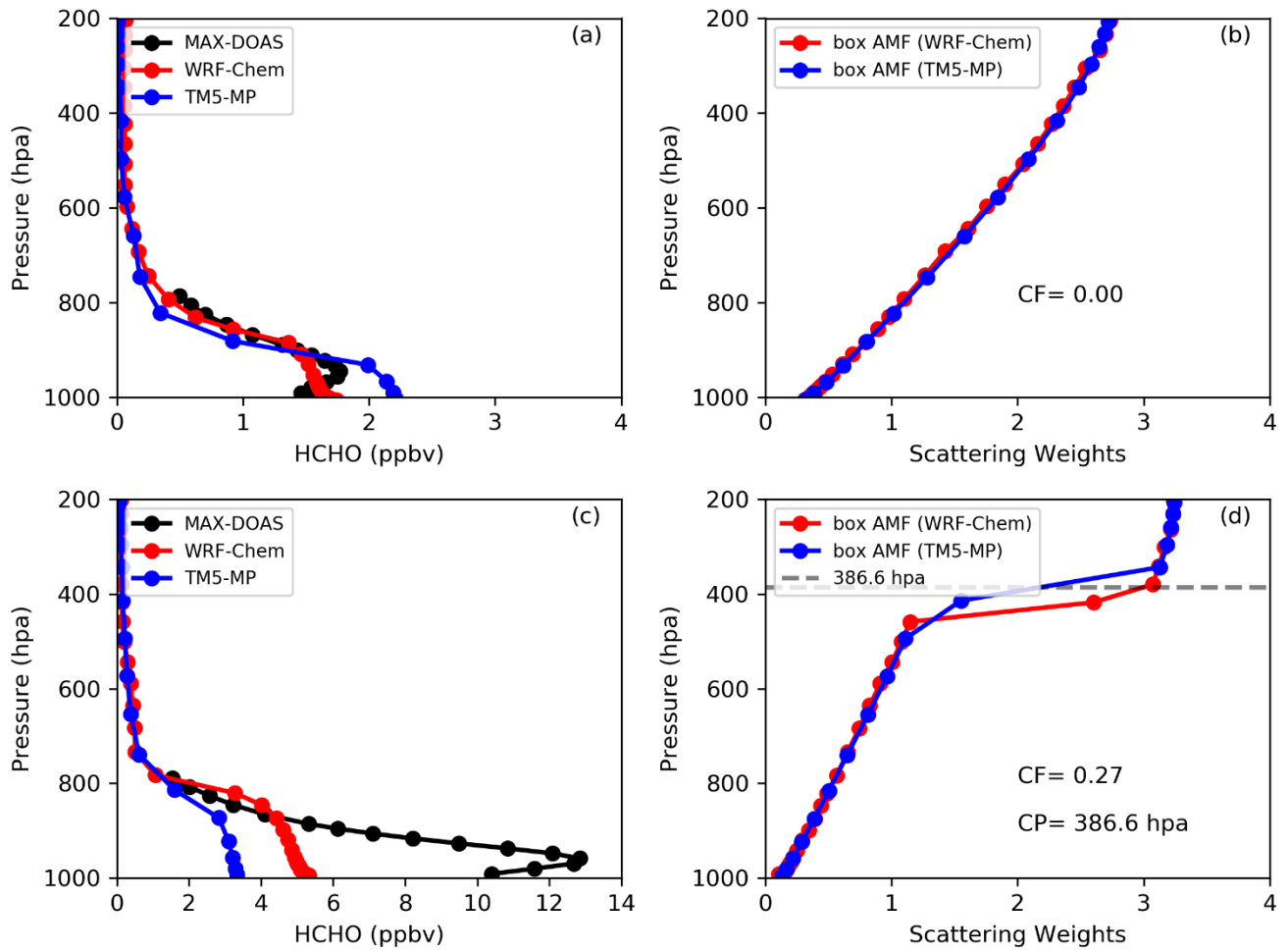
750

Figure 6. Daily averaged vertical HCHO profiles obtained from MAX-DOAS, WRF-Chem and TM5-MP model in clean case on 03 March 2019 (a) and in polluted case on 26 June 2019. Comparisons of box AMF using WRF-Chem and TM5-MP simulations in clean case with clear sky on 03 March 2019 (b) and in polluted case with cloudy sky on 26 June 2019 (c). The locations of two pixels are within 20 km of the CAMS site.
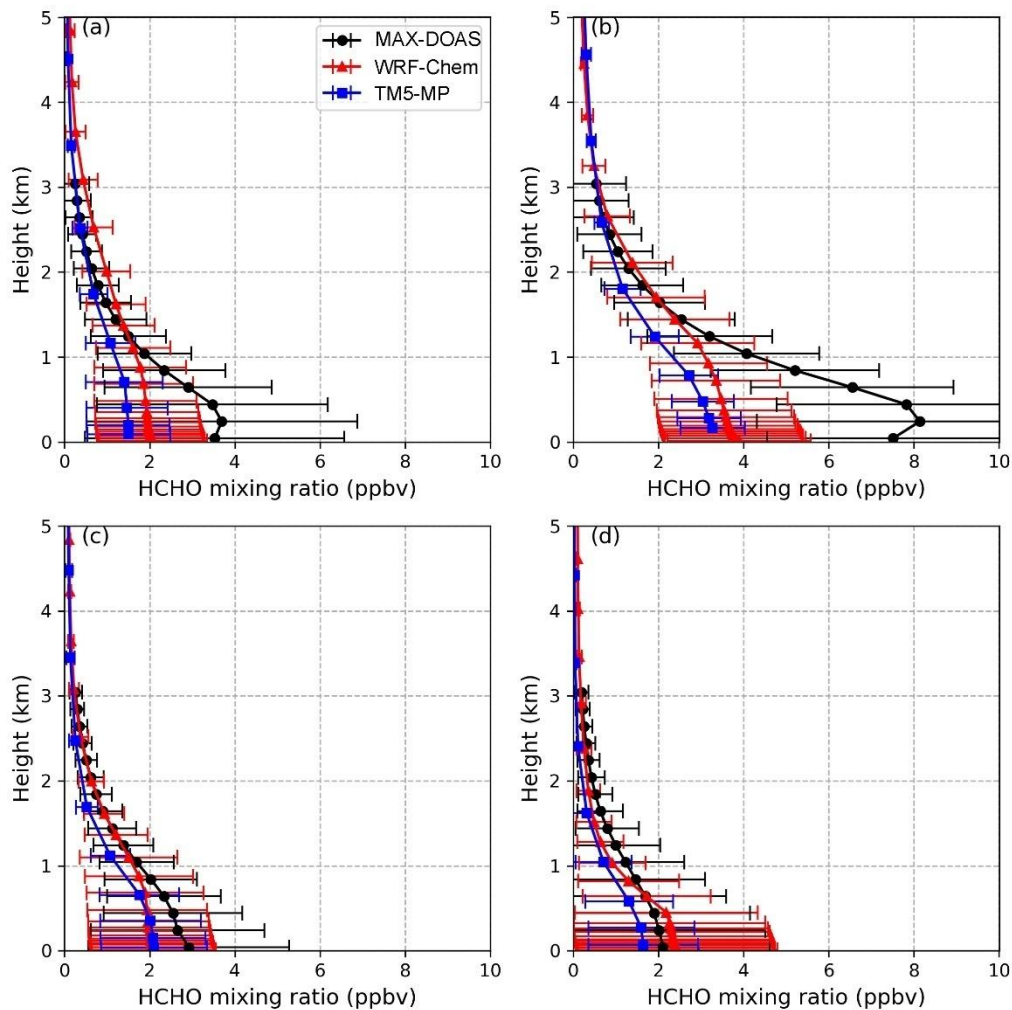
755

Figure 7. Seasonal average of vertical HCHO profiles obtained from MAX-DOAS, WRF-Chem and TM5-MP model in spring (a), summer (b), autumn (c) and winter (d) at CAMS site. The error bars represent 1σ standard deviation of variation.
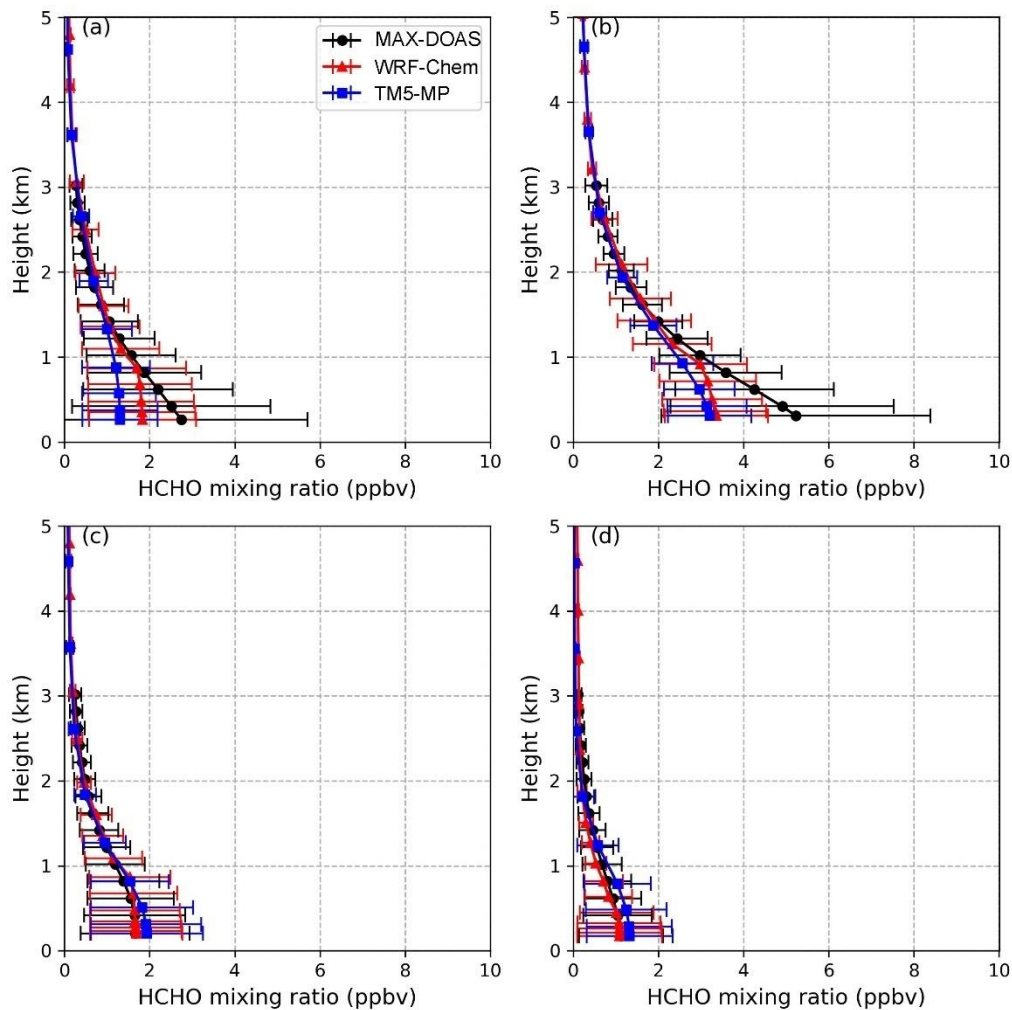
Figure 8. Seasonal average of vertical HCHO profiles obtained from MAX-DOAS, WRF-Chem and TM5-MP model in spring (a),
760   **summer (b), autumn (c) and winter (d) at UCAS site. The error bars represent 1σ standard deviation of variation.**
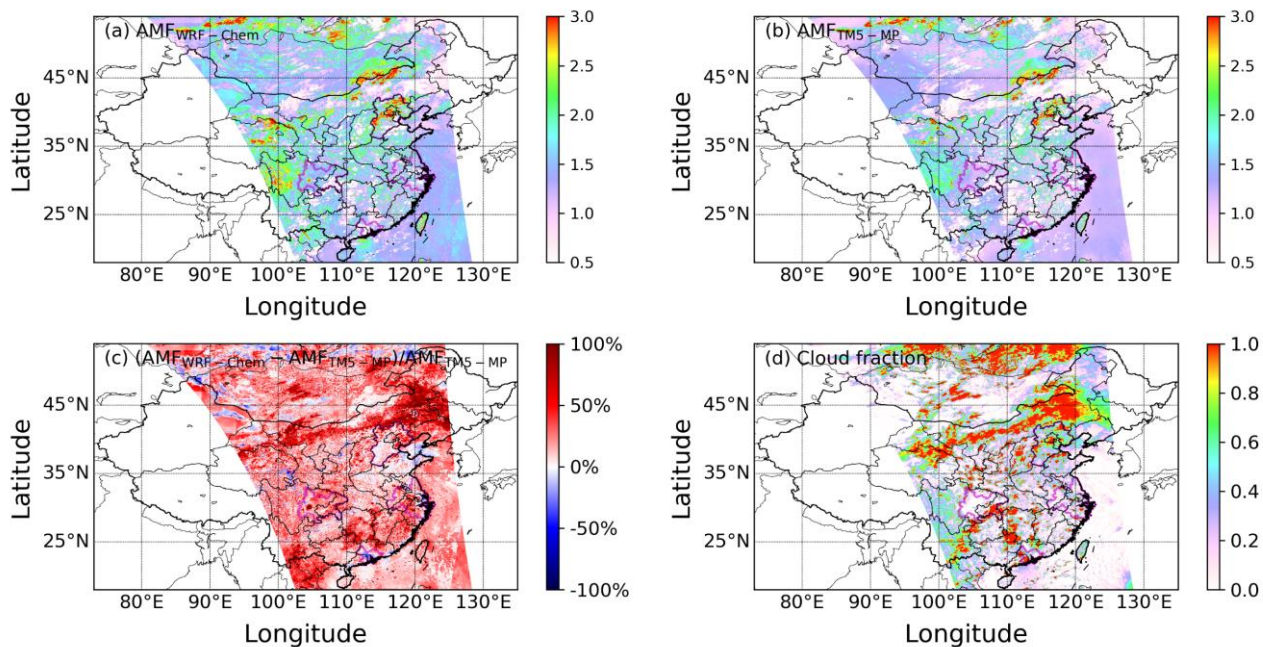
Figure 9. Spatial distributions of AMFs calculated using WRC-Chem (a) and TM5-MP (b) simulations as a priori HCHO profiles of orbit 04211 on 06 August 2018. Spatial distribution of difference of the AMFs (c) and of cloud fraction (d) of orbit 04211 on 06 August 2018.
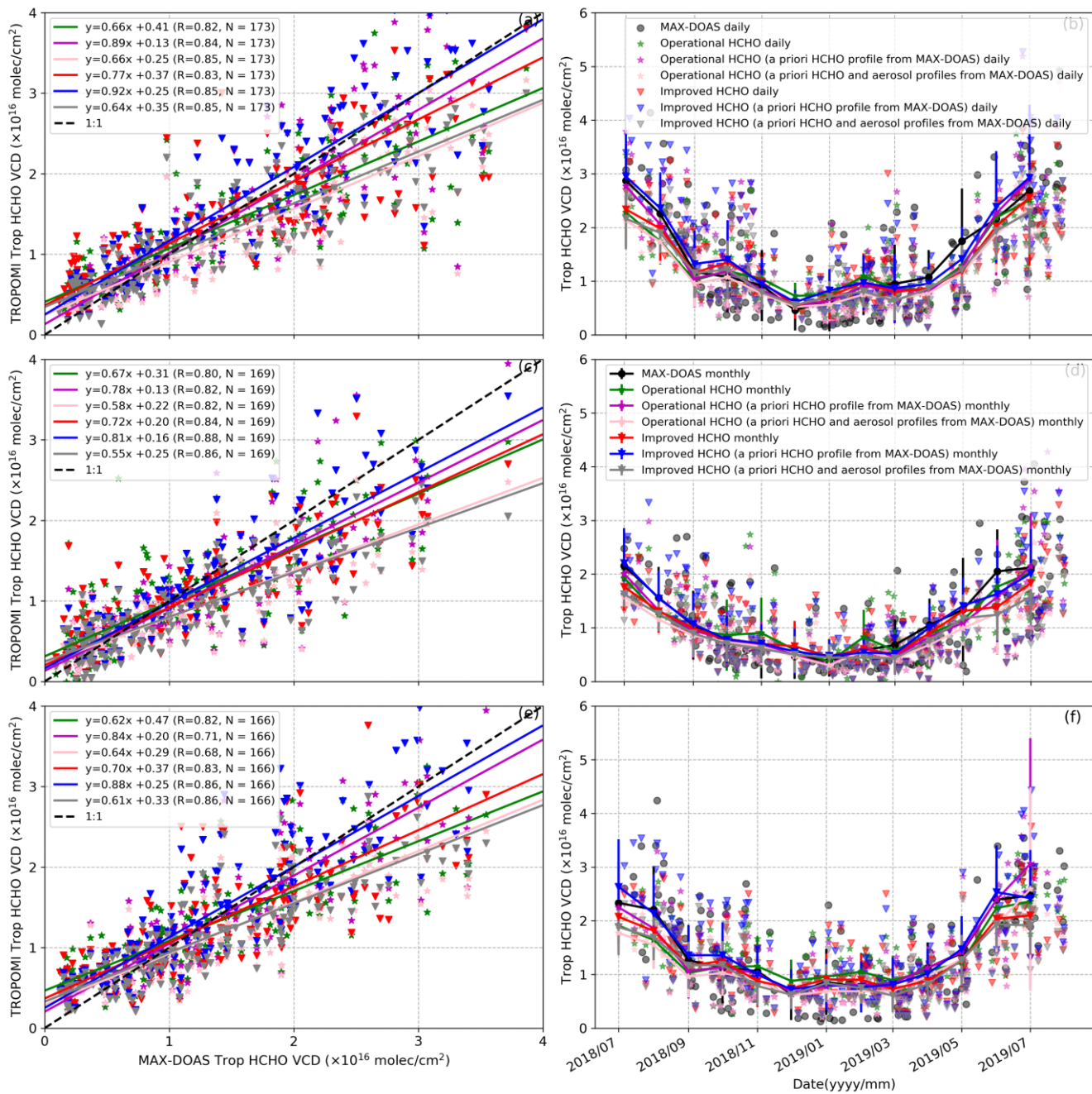
Figure 10. Comparison of tropospheric HCHO VCDs between TROPOMI and MAX-DOAS measurements from July 2018 to July 2019 at CAMS (a), UCAS (c) and NC (e) sites. Time series of TROPOMI and MAX-DOAS tropospheric HCHO VCDs from July 2018 to July 2019 at CAMS (b), UCAS (d) and NC (f) sites.
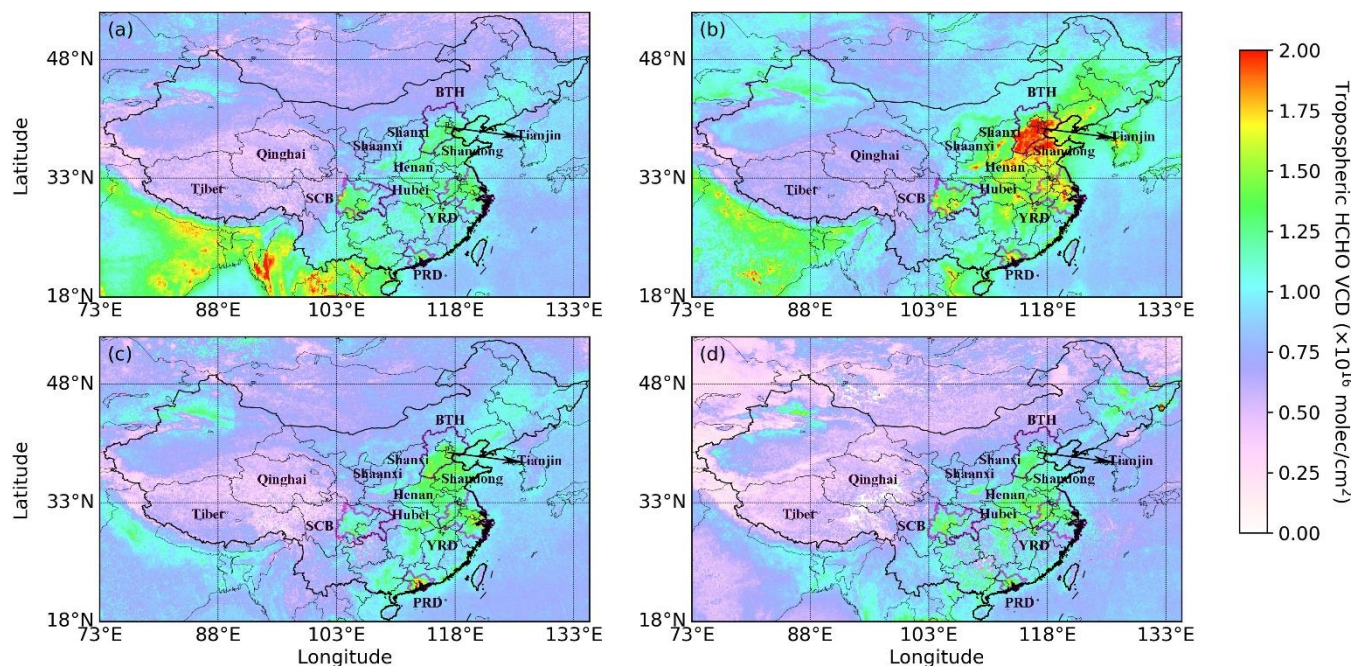
Figure 11. The spatial distribution of average tropospheric HCHO VCDs over China on a 0.1°×0.1° grid in spring (a), summer (b), autumn (c) and winter (d).
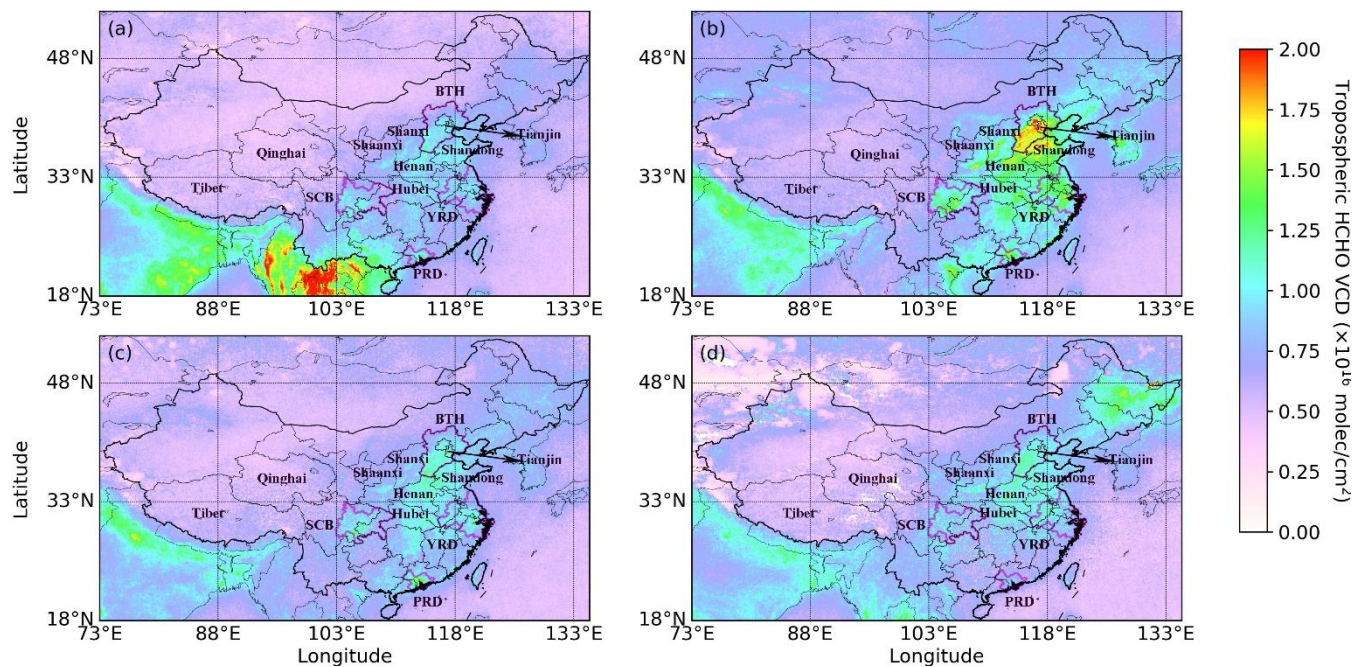
Figure 12. The spatial distribution of average TROPOMI operational tropospheric HCHO VCDs over China on a 0.1°×0.1°grid in spring (a), summer (b), autumn (c) and winter (d).